

## Mean Structure and Dynamics of the Shelfbreak Jet in the Middle Atlantic Bight during Fall and Winter\*

P. S. FRATANTONI, R. S. PICKART, D. J. TORRES, AND A. SCOTTI<sup>+</sup>

*Department of Physical Oceanography, Woods Hole Oceanographic Institution, Woods Hole, Massachusetts*

(Manuscript received 9 February 2000, in final form 9 October 2000)

### ABSTRACT

Using a collection of high-resolution shipboard acoustic Doppler current profiler (ADCP) velocity sections that cross the Middle Atlantic Bight shelfbreak jet near 70°W, the mean structure of the frontal jet is described and the dominant modes of variability of the jet are examined. A mean section is constructed in a translating coordinate frame whose origin tracks the instantaneous position of the core of the jet, thereby minimizing variability associated with the lateral meandering of the current. The mean jet so constructed extends to the bottom, tilting onshore with depth, with near-bottom flow exceeding 0.10 m s<sup>-1</sup>. The corresponding cross-stream flow reveals a clear pattern of convergence that extends along the tilted axis of the jet, with enhanced convergence both near the surface and near the bottom. This convergence is largely attributed to the locally convergent topography and is shown to drive an ageostrophic circulation dominated by downwelling at, and offshore of, the jet core. The collection of ADCP sections also suggests a previously undetected mode of variability, whereby the jet systematically fluctuates between a convergent, bottom-reaching state and a surface-trapped state with weaker cross-stream velocities. This variability is associated with significant variations in the southwestward transport of the jet and does not seem to be related to simple meandering of the current.

### 1. Introduction

The shelfbreak front of the Middle Atlantic Bight (MAB) is a persistent thermohaline front that separates relatively cold and fresh shelf waters from warm, salty waters on the continental slope. Coincident with the front is a narrow jet, which has been estimated to transport approximately 0.2–0.3 (Sv  $\equiv 10^6$  m<sup>2</sup> s<sup>-1</sup>) of water equatorward south of New England (Linder and Gawarkiewicz 1998). This shelfbreak frontal jet is part of a larger-scale buoyancy driven coastal current system that originates in the Nordic domain as the East Greenland Current, winds cyclonically around the perimeter of the Labrador Basin, exiting the basin as the Labrador Current, and flows adjacent to the Grand Banks of Newfoundland before entering the subtropical domain (Chapman and Beardsley 1989). Throughout its path the current is subject to different sources and sinks, though overall it experiences a loss of transport (Loder et al. 1998). The shelfbreak jet is an important component of

the coastal environment in the northwest Atlantic. The front and jet represent a semipermeable barrier that limits the exchange of waters between the shelf and open ocean. The cross-shelf exchange that does occur strongly impacts the spreading of coastal contaminants and is of leading importance in the freshwater budget on the shelf. Hence, in order to quantify the shelf/slope exchange of mass and tracers, we need to understand fully both the mean and time-varying aspects of the jet.

The MAB shelfbreak front and current have been described in numerous studies over the past 50 years, utilizing a combination of observations which include repeat hydrographic surveys (e.g., Beardsley and Flagg 1976), historic climatologies (Linder and Gawarkiewicz 1998), and long-term moored current meter and thermistor arrays [e.g., Nantucket Shoals Flux Experiment (NSFE), Beardsley et al. 1985; Shelf Edge Exchange Processes (SEEP-I), Aikman et al. 1988]. Results from these studies have illustrated the sensitivity of the shelfbreak jet and front to a large number of forcing mechanisms, all of which can result in different jet configurations. In general, hydrographic sections are limited to the cross-transect component of the flow, can be subject to severe aliasing [e.g., internal waves, Burrage and Garvine (1987)], and provide only the baroclinic geostrophic contribution. By comparison, moored velocity arrays provide absolute velocity measurements with high temporal resolution but have been unable to resolve completely the horizontal current structure. Therefore,

\* WHOI Contribution Number 10130.

<sup>+</sup> Current affiliation: Department of Marine Sciences, University of North Carolina, Chapel Hill, North Carolina.

Corresponding author address: P. S. Fratantoni, Physical Oceanography Dept., Woods Hole Oceanographic Institution, MS 21, Woods Hole, MA 02543.  
E-mail: E-mail: pfratantoni@whoi.edu

the jet has yet to be simultaneously fully resolved in (cross-stream) space and time.

The most comprehensive description of the mean structure of the MAB shelfbreak front and jet is given by Linder and Gawarkiewicz (1998), who created a two-dimensional climatology of the shelfbreak front for the winter and summer seasons. Their results nicely illustrate the seasonal progression of the density front from a top to bottom feature in winter to a front that is isolated from the surface in summer by a seasonal pycnocline. The geostrophic jet associated with these frontal gradients is on the order of  $0.15\text{--}0.20\text{ m s}^{-1}$ . However, this is a long-term average representation of the jet, using data over a 90-yr period, and it uses nonconcurrent velocity data for referencing.

The shelfbreak jet is influenced by both external and internal forcing mechanisms. Theoretical studies (Flagg and Beardsley 1978; Gawarkiewicz 1991; Lozier et al. 2001, manuscript submitted to *J. Phys. Oceanogr.*) and observations (Linder and Gawarkiewicz 1998) have shown that the jet structure is inherently baroclinically unstable. This internal forcing may lead to finite-amplitude meanders that propagate along the axis of the jet (Halliwell and Mooers 1979) and occasionally develop into frontal eddies (Houghton et al. 1986; Garvine et al. 1988). In addition, the jet may be influenced by external forcing mechanisms such as local winds (Houghton et al. 1988) and upstream variations in the source water (Chapman and Beardsley 1989; Petrie and Drinkwater 1993). Another important external influence on the jet is due to the circulation of the adjacent slope water. For instance, the close proximity of the Gulf Stream south of New England results in a fair number of anticyclonic Gulf Stream rings impinging on the continental slope in the MAB. It remains unclear what role Gulf Stream rings play in the variability at the shelf break. Beardsley et al. (1985) report that subtidal fluctuations forced by the passage of Gulf Stream rings over the upper continental slope are not correlated with fluctuations observed over the shelf, suggesting that the shelf break can be a transition region for forcing. Ramp et al. (1983) demonstrated that the presence of Gulf Stream rings enhances cross-shelf velocity gradients in the vicinity of the shelfbreak jet and can lead to the excitation of waves due to horizontal shear instabilities. Observations also suggest that the interaction of Gulf Stream rings with the shelfbreak jet may transport significant volumes of shelf water into the slope region (Joyce et al. 1992). However, it is still unclear how often rings simply alter the path of the shelfbreak jet (e.g., Pickart et al. 1999b) versus permanently exporting water from the shelf.

Until recently there were no direct high-resolution velocity measurements of the shelfbreak jet. Instead, information about the structure of the jet was derived from current meters, which were limited in spatial resolution, or from hydrographic data, which provide only the cross-transect component of the baroclinic flow

field. Using long-term moored arrays, two observational programs (SEEP-I and NSF-E) significantly advanced our understanding of the long-term statistics of the velocity and temperature structure over the shelf and slope. The results demonstrated that the mean flow field included a surface-intensified westward flowing jet at the shelf break (Aikman et al. 1988). It was also demonstrated that the shelfbreak density front, as well as the overall currents, were sensitive to seasonal changes in the strength of the wind forcing (Beardsley et al. 1985; Aikman et al. 1988; Houghton et al. 1988). More recently, vessel-mounted acoustic Doppler current profilers (ADCPs) have provided high-resolution, two-dimensional velocity sections of the shelfbreak current (e.g., Gawarkiewicz et al. 1996; Barth et al. 1998; Pickart et al. 1999b). While these observations are still simply snapshots in the ever-changing evolution of the shelfbreak current, they have provided the first detailed information on both the primary (alongstream) and secondary (cross-stream) circulation associated with the jet.

In this paper, a collection of highly resolved shipboard ADCP velocity sections, taken across the shelfbreak jet over a period of two years, has been combined into a two-dimensional mean description of the shelfbreak jet. We have limited our analysis to winter and fall because of the apparent changes in jet structure and variability that result from the formation of a seasonal pycnocline. In order to describe the structure of the jet in isolation from spatial variations due to the meandering of the current, we have adopted a methodology previously applied to velocity observations in the Gulf Stream (Halkin and Rossby 1985). In this method, the velocity sections are averaged with respect to a translating coordinate system that is aligned with the high velocity core of the jet, the so-called streamwise coordinate method. This minimizes any smoothing due to lateral translations of the jet. The result is a first glimpse of the detailed mean structure of the shelfbreak jet in the MAB during the winter and fall. Results indicate that the local topography plays a major role in dictating the structure of the jet, as well as in the dynamics of its secondary circulation.

By analyzing the ensemble of velocity sections in streamwise coordinates, we are also able to quantify the variability associated with the cross-stream structure of the jet over the 2-yr period. Employing the method of empirical orthogonal function analysis, a heretofore undetected mode of variability emerges which appears to be associated with significant changes in the transport of the jet. Although previous studies indicate that current meandering (be it internally or externally forced) is prevalent throughout the MAB, the characteristics of the variability observed here suggest that simple meandering is not the cause.

## 2. ADCP data and methods

As part of the recent Shelfbreak PRIMER Experiment to investigate the shelf/slope circulation in the MAB

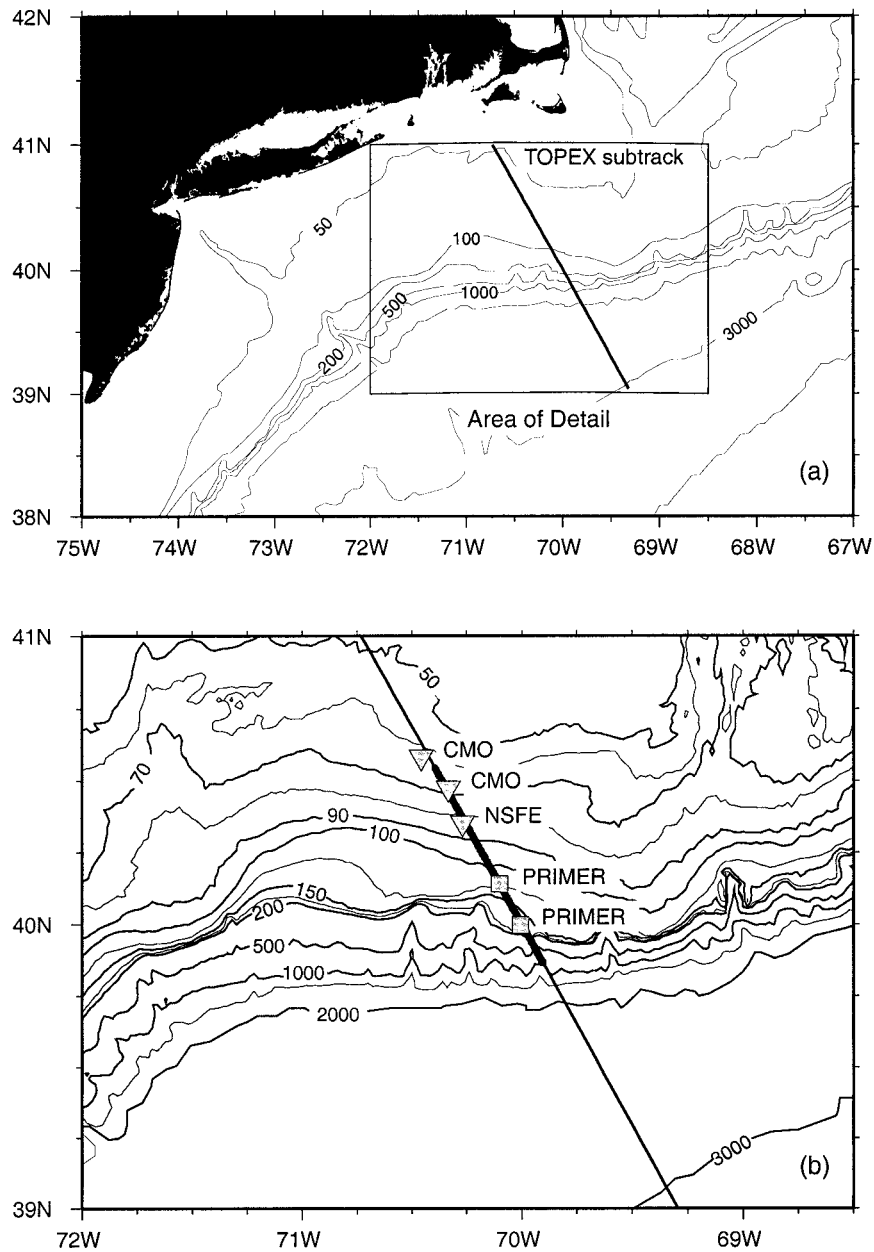


FIG. 1. (a) The study region south of Nantucket, Massachusetts. The TOPEX altimeter subtrack C126 is shown. (b) The heavy black line shows the location and horizontal extent of the repeat shipboard ADCP surveys. The inverted triangles denote the location of three current meter moorings whose velocity records were used, together with velocity observations from two upward-facing ADCPs (squares), to predict the barotropic tide along the survey line.

south of New England (see Pickart et al. 1999b for details), a repeat survey line was established across the shelfbreak jet coincident with the TOPEX altimeter subtrack near 70°W (Fig. 1). The orientation of the survey line was chosen to compliment the remote sensing component of the PRIMER experiment (namely the long-term monitoring of the shelfbreak frontal jet and slope water currents) with hopes that in situ observations could be used to ground truth the altimetric data. However, to date, the sea surface height data at the shelf

break has proven elusive to interpret and therefore will not be addressed in this paper. Two upward-looking ADCPs were moored near the shelf break on the survey line for most of the shipboard survey period (Fig. 1). The line was occupied numerous times over the course of two years between December 1995 and December 1997, resulting in ten separate highly resolved shipboard ADCP velocity realizations of the shelfbreak jet (Table 1).

The velocity data spanned all of the seasons, but only

TABLE 1. Shipboard ADCP surveys crossing the shelfbreak jet. Coincident temperature ( $T$ ) and salinity ( $S$ ) measurements are denoted in the right column.

Jet cross- ing	Survey dates	Season	Resolution (m)		Hydro- graphy
			Vertical	Horizon- tal	
1	5–6 Dec 1995	Winter	8	1500	$T$
2	9 Dec 1995	Winter	4	500	$T, S$
3	5–6 May 1996	Spring	4	270	$T, S$
4	5–6 Aug 1996	Summer	8	340	$T, S$
5	2–3 Nov 1996	Fall	8	680	—
6	3 Nov 1996	Fall	8	400	$T, S$
7	21–28 Feb 1997	Winter	8	540	$T, S$
8	13–14 Jun 1997	Summer	4	650	—
9	14 Jun 1997	Summer	4	1300	$T, S$
10	5–6 Dec 1997	Winter	8	680	—

three of the sections were occupied during the summer. In summer, the regional stratification is significantly altered by the development of a seasonal pycnocline, and while much is known about the winter to summer transition of the shelfbreak property front, very little is known about any corresponding changes in the jet structure and variability. In the three summer shipboard ADCP crossings, the jet had a subsurface core centered around 40-m depth, quite different than the nonsummer surface-intensified core. While the Linder and Gawarkiewicz (1998) climatology shows no such seasonally varying structure, the summertime jet core observed here is consistent with observations from multiple ADCP crossings completed just downstream of our survey line during the PRIMER experiment (G. Gawarkiewicz 2000, personal communication). Additionally, model results indicate that the stability characteristics of the shelfbreak jet are significantly altered by the inclusion of a seasonal pycnocline (Gawarkiewicz 1991), with the most unstable wave being surface-trapped during winter conditions and pycnocline-trapped during summer stratified conditions. These observations and model results suggest that the development of a seasonal pycnocline may significantly alter the basic structure and variability of the jet. For this reason, only the nonsummer realizations of the jet are included in the present study. Since the conclusion of the PRIMER experiment, we have obtained 12 more “ship of opportunity” summertime reoccupations of the survey line; hence a future study will investigate the summer structure and variability of the shelfbreak jet.

Before individual velocity sections could be combined to form a mean shelfbreak section, several sampling issues needed to be addressed. First, the shipboard ADCP measures both the ageostrophic and the geostrophic components of the flow. Because the shelfbreak jet resides in the upper 200 m of the water column, the velocity measurements include potentially significant contributions from the tides and inertial oscillations. Although it has been shown that the barotropic tidal amplitudes in this region are typically only 10%–15% of

the core speed of the shelfbreak jet (Pickart et al. 1999b), such tidal amplitudes and inertial amplitudes can be of the same order as the secondary circulation in the jet (cross-stream flow). Efforts to remove the barotropic tides from the velocity sections and to estimate the effect of the baroclinic tides and inertial oscillations are discussed in section 2a. Second, although the velocity sections were all occupied along the same TOPEX line, this line is not oriented normal to the local isobaths and hence not normal to the expected mean direction of the shelfbreak jet. For this reason, a rotated coordinate system was defined for each occupation based on the direction of the shelfbreak jet at the time of the survey. The methodology for this is described in section 2b. Finally, when using a shipboard ADCP, acoustic interference near the bottom limits the vertical current profile to a maximum range of 85% of the total water column depth. Therefore, the reader should keep in mind that “near-bottom” is intended to mean approximately 15 m off of the bottom.<sup>1</sup> We do not resolve the bottom boundary layer with these measurements. Similarly, acoustic interference near the hull of the ship contaminates velocity observations within 17 m of the surface. Therefore, in the results to follow, we limit the current profiles to depths greater than 20 m.

#### a. Tides and inertial oscillations

One of the difficulties inherent in working with in situ velocity measurements of the shelfbreak jet is that they are subject to potentially strong tidal and inertial oscillations. Fortunately, this part of the MAB corresponds to a regional minimum in the semidiurnal barotropic tidal energy (Twichell et al. 1981; Moody et al. 1984), decreasing the likelihood of tidal interaction, and hence resulting in similarly small baroclinic tides and mixing. Both to the east and west of our site the combination of coastline geometry and shelf width make the tidal system more resonant at the semidiurnal frequencies, resulting in significantly larger tidal amplitudes (e.g., Garrett 1972). Hence, in this respect, our survey line is optimally located.

The relative strengths of the barotropic and baroclinic tides were estimated using the yearlong velocity time series from the shelfbreak ADCP moorings. The velocity time series were high-pass filtered using a second-order Butterworth filter with a 40-h cutoff and decomposed into their barotropic and baroclinic components. The filtered velocities from each mooring were vertically averaged to create a time series of barotropic velocities. It should be noted that because the range of the moored ADCP is limited by acoustic interference near the surface, what we are calling the barotropic component of the flow is only representative of the true

<sup>1</sup> Because of the robust signals at depth, we have in fact extrapolated velocities into this region (indicated by the shaded area in all figures).

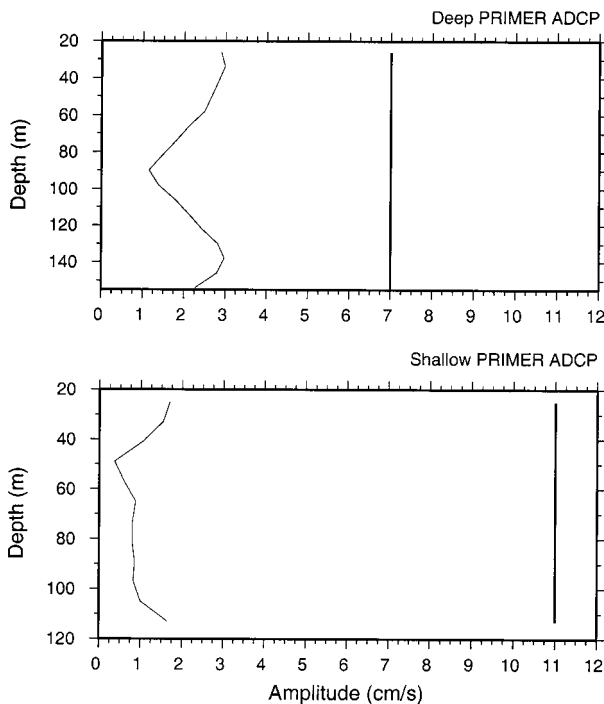


FIG. 2. The relative amplitude of the barotropic (heavy line) and baroclinic (light line) components for the  $M_2$  tidal constituent as determined from the moored shelfbreak ADCPs in Fig. 1.

barotropic flow determined using a full water-column average. The barotropic velocities were subtracted from the original record to obtain a time series of baroclinic velocities. The coefficients for the dominant tidal constituents were calculated using a simple least squares technique and tidal ellipses were constructed to determine the amplitude and phase of each tidal constituent. The relative amplitudes of the barotropic and baroclinic components of the  $M_2$  tidal constituent (which dominates the local tidal currents) are compared in Fig. 2. The vertical structure of the amplitude of the  $M_2$  baroclinic tide has a first mode character with the surface layer  $180^\circ$  out of phase with the lower layer (not shown). More importantly, however, the amplitude of the  $M_2$  baroclinic tide, ranging between  $0.01$ – $0.03 \text{ m s}^{-1}$  in this region, is up to an order of magnitude smaller than the barotropic tide, which ranges between  $0.07$ – $0.11 \text{ m s}^{-1}$ . These results suggest that the baroclinic tide is small compared with the barotropic tide in this region of the MAB. Further, the amplitude of the baroclinic tide is small enough, compared with the amplitudes of the alongstream and cross-stream velocities in the shelfbreak jet, that the general flow patterns of the jet are robust (i.e., flow reversals and convergent/divergent patterns; cf. Fig. 3).

Although the barotropic tides are relatively small in this region, we are able to reduce their effects even more by utilizing velocity records from a collection of long-

term moorings spanning the TOPEX line. In addition to the two moored shelfbreak PRIMER ADCPs, two heavily instrumented current meter moorings were deployed along the inshore portion of the TOPEX line as part of a concurrent program (The Coastal Mixing and Optics Experiment; Galbraith et al. 1999). These moored velocity measurements, together with historical velocity observations collected during NSF-E, encompass the horizontal domain sampled by the shipboard ADCPs, affording us the opportunity to accurately predict and remove the barotropic tide from each of our shipboard velocity sections (Fig. 1). These time series have been used to predict the amplitude of the 13 dominant barotropic tidal constituents across the domain and to remove the barotropic tidal signal from each of the shipboard sections (see appendix). The tidal prediction algorithm results in the removal of a significant portion of the energy at the dominant tidal frequencies. For example, detiding the moored shelfbreak PRIMER ADCP velocity time series resulted in an 80% reduction in the energy contained in the semidiurnal frequency band. The amplitude of the residual currents in the  $M_2$  frequency band was  $0.02 \text{ m s}^{-1}$ , small with respect to the velocities in the shelfbreak jet.

Figure 3 illustrates the effects of detiding on a single velocity section, the third occupation in Table 1. As one might expect, the structure of the alongstream component of the jet is not significantly altered by the removal of the barotropic tides (Fig. 3, left).<sup>2</sup> In the case shown, the shelfbreak jet has been sharpened by the detiding into a well-defined region of westward flow that extends all the way to the bottom. The detiding has a greater impact on the structure of the cross-stream velocity field (Fig. 3, right). In the example presented here, the detided cross-stream velocity field reveals a convergent pattern centered along the vertical axis of the alongstream jet. Overall, the detiding resulted in sharpened velocity gradients, intensified alongstream velocities, and more organized cross-stream flow patterns.

Inertial oscillations represent another source of error in the analysis of in situ velocity measurements of the shelfbreak jet. The strength of the inertial oscillations along the TOPEX line was estimated using the velocity time series from the deeper of the two shelfbreak PRIMER ADCPs, as its record was longer and contained no interruptions unlike the shallower ADCP (Fig. 1). First, the moored velocity time series was detided using the tidal coefficients from the prediction algorithm described in the appendix. Complex demodulation was then applied to the detided time series in order to estimate the amplitude and phase of the velocity fluctuations at the inertial frequency (18.8 h) as a function of time. The mean amplitude profile (calculated over the yearlong deployment) was surface and bottom intensified (Fig. 4a). The

<sup>2</sup> The velocity fields are presented in a rotated coordinate frame whose alongstream component is parallel to the flow at the core of the shelfbreak jet (see section 2b).

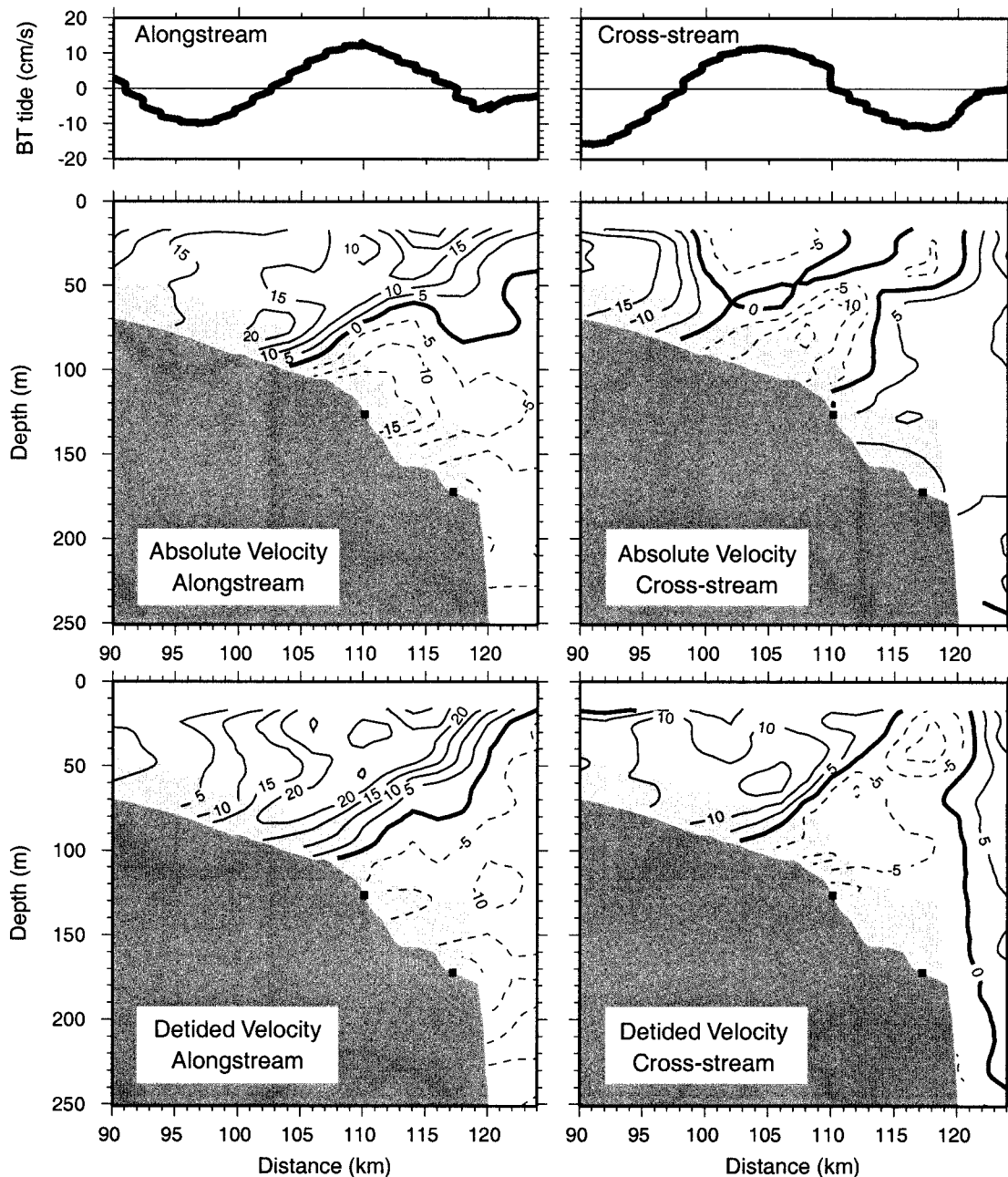


FIG. 3. Comparison of a single absolute alongstream and cross-stream velocity section as measured by the shipboard ADCP (middle) with the corresponding detided velocity section (bottom) after the barotropic tides have been removed. The velocity fields are presented in a rotated coordinate frame whose alongstream component is parallel to the flow at the core of the shelfbreak jet (see section 2b). The section shown is the third occupation in Table 1. The solid contours represent equatorward flow in the alongstream fields and offshore flow in the cross-stream fields. The amplitude of the barotropic tide, which was removed across each section is also shown (top). The shaded region near the bottom represents the region where no data exist and velocities are extrapolated. There is a blanked region near the surface due to the acoustic interference near the hull of the ship.

mean amplitude was approximately  $0.06 \text{ m s}^{-1}$  near the surface and bottom and decreased to a minimum amplitude of  $0.04 \text{ m s}^{-1}$  at roughly 80 m. These magnitudes are consistent with the inertial amplitudes reported by Beardsley et al. (1985). The strength of the inertial os-

cillations was also estimated from the amplitude time series during each of the shipboard ADCP occupations and compared to the magnitude of the alongstream and cross-stream velocities in the shelfbreak jet at that time. In general, the inertial amplitudes were significantly less

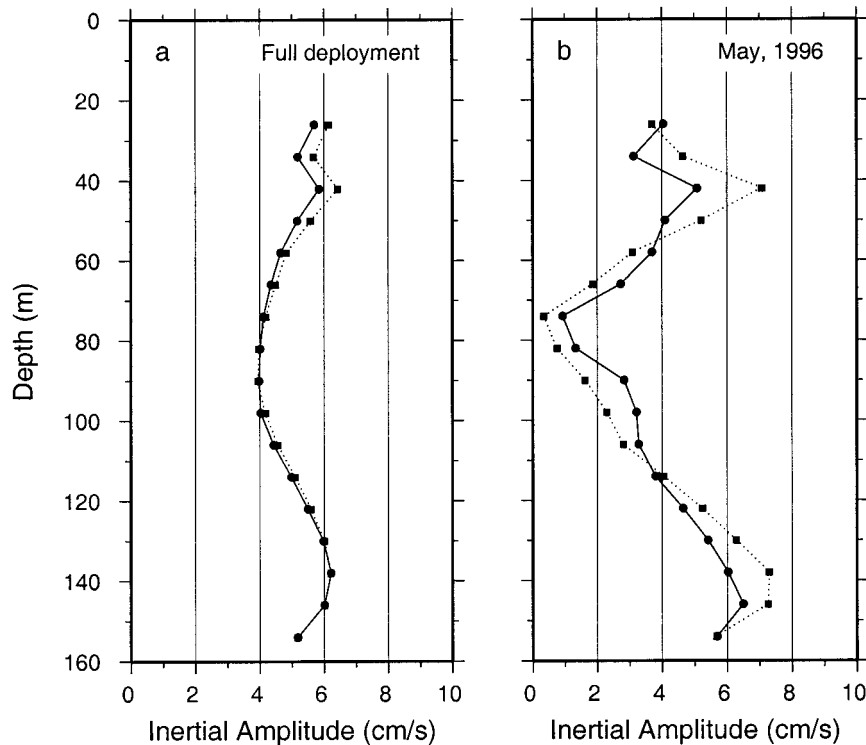


FIG. 4. (a) The deployment mean amplitude of the inertial oscillations as measured by the offshore shelfbreak ADCP. (b) The mean amplitude of the inertial oscillations calculated over the period coinciding with the third shipboard survey (Fig. 3). The solid lines represent the east–west component while the dotted lines represent the north–south component of the flow.

than the alongstream and cross-stream velocity signals of interest. For example, during the third occupation (Table 1, Fig. 4b) the average inertial amplitudes were  $0.03\text{--}0.04\text{ m s}^{-1}$  within the upper 100 m where the alongstream and cross-stream jet amplitudes exceed  $0.30\text{ m s}^{-1}$  and  $0.15\text{ m s}^{-1}$ , respectively (Fig. 3).

In summary, the moored ADCP time series revealed that the baroclinic tides, inertial oscillations, and residual barotropic tides (after detiding) are smaller than the primary and secondary jet amplitudes over most of the water column. In general, flow patterns, specifically flow reversals associated with convergent/divergent flow regimes, are robust in the face of tides and inertial oscillations. Without exception, the removal of the barotropic tides from each of the shipboard velocity sections resulted in a more plausible jet structure. Hence, we are confident that this collection of shipboard ADCP sections accurately captures the subtidal velocity signal of the MAB shelfbreak jet.

#### b. Coordinate frames

Halkin and Rossby (1985) developed a method for diagnosing the mean structure, transport, and variability of the Gulf Stream while minimizing the influence of lateral meandering of the current. They accomplished this by transforming the velocity observations into a translating coordinate system whose origin tracks the

core position of the current. In this streamwise coordinate system, the major axis is aligned parallel to the overall downstream direction of the current while the origin of the coordinate system is defined so that its geographical position varies with the position of the core of the current. Here, a similar method is employed to describe the mean structure of the shelfbreak jet and to diagnose its variability while minimizing the effects of cross-shelf meandering. The ensemble of velocity sections is also analyzed in fixed geographic coordinates in order to examine the impact of the meandering on the structure and variability of the shelfbreak current.

Our sampling occurred along a line that is not oriented directly normal to the isobaths (Fig. 1) and hence not perpendicular to the expected mean direction of the shelfbreak jet. Before analyzing the velocity observations in either geographic or stream coordinates, the velocities were first rotated into an along- and cross-stream coordinate system and the station locations were projected onto the new cross-stream axis. This ensures that the following analysis is unaffected by changes in the orientation of the current relative to the survey line. The alongstream direction of the jet was determined for each realization by the mean (20–50 m) transport vector averaged over the  $e$ -folding width of the jet (Fig. 5a). Inherent in this methodology is the assumption that the structure of the shelfbreak jet remains largely the same over the alongstream distance sampled in each reali-

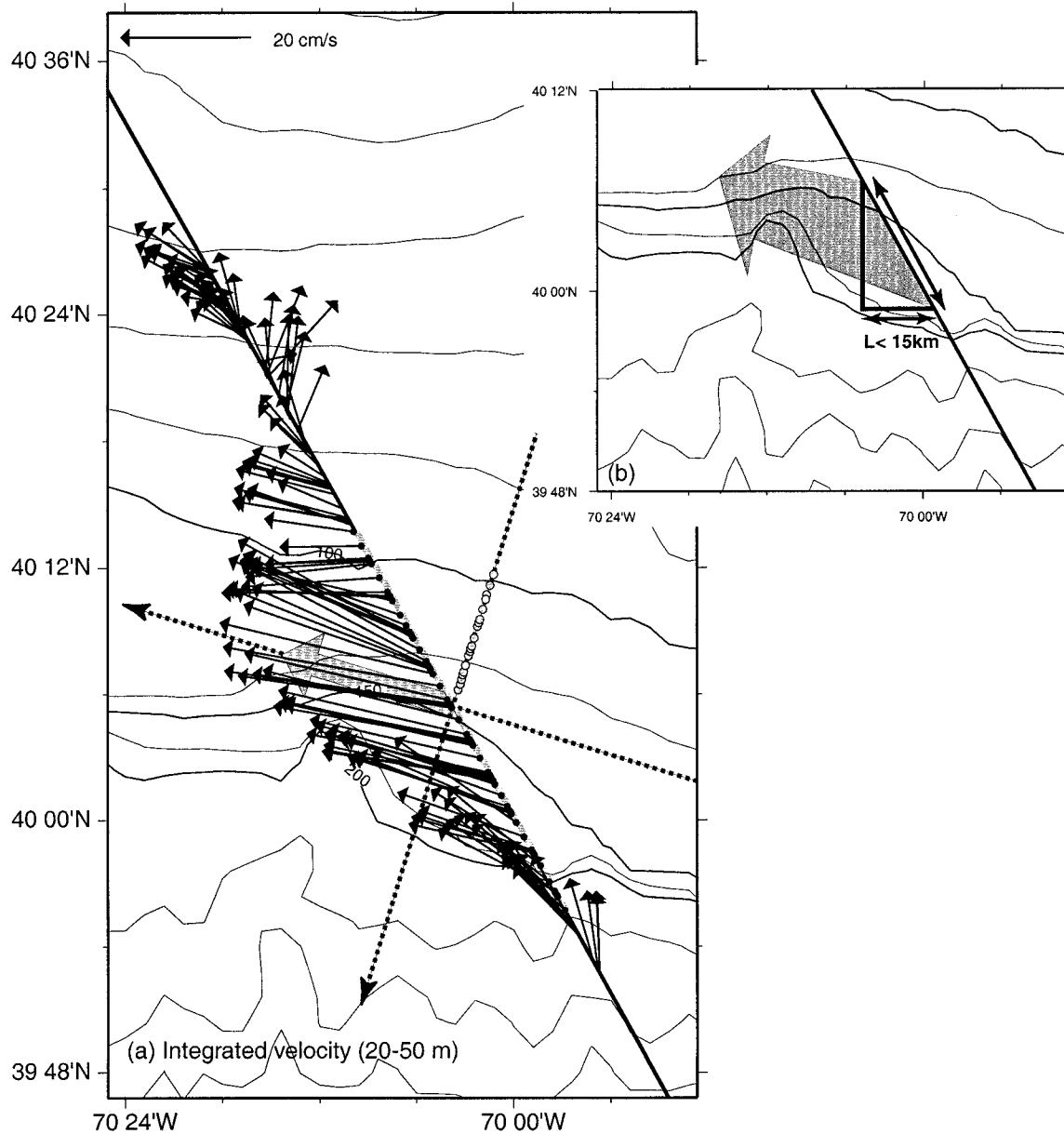


FIG. 5. (a) The velocity integrated over the upper 50 m of the water column from the first shipboard survey. The gray shaded arrow represents the location and orientation of the mean transport vector averaged over the  $e$ -folding width of the jet (denoted by the gray shading along the survey line). The streamwise coordinate system is overlaid (dashed vectors) with the origin defined by the maximum transport vector. The gray circles on the cross-stream coordinate axis represent the projection of the station positions as a result of the coordinate rotation (the stations projected south of the mean jet axis are not shown). The inset panel (b) illustrates the alongstream distance that is sampled while crossing the  $e$ -folding width of the jet.

zation (inset Fig. 5b). The degree to which this is not true represents a source of error that is dependent on the width of the jet and the angle at which the jet intersects the survey line. This alongstream distance has been estimated for each jet crossing based on the width of the instantaneous jet and the intersecting angle of the jet with respect to the survey line. The majority of the realizations sample a distance less than 15 km in the

alongstream direction. By comparison, the alongstream length scale associated with frontal meanders and eddies in the shelfbreak jet range from 20 to 35 km (Garvine et al. 1988; Ramp et al. 1983). While our sampling distance is smaller than the scales of observed along-lope variability, it is nonetheless a source of ambiguity and should be kept in mind when interpreting the velocity fields to follow. In the rotated coordinate system

and subsequent results, the positive  $x$  axis is aligned parallel to the downstream direction of the jet (equatorward) while the  $y$  axis is positive in the offshore direction.

The only difference between the geographic coordinate system and the stream coordinate system is the location of the origin of the coordinate axes. In the former, the origin is fixed at a given location. For the geographic frame of reference we used a bottom-depth versus height above bottom coordinate system. After the transformation to bottom-depth coordinates, each velocity section was gridded using Laplacian-spline interpolation onto a regular grid with 10-m spacing in bottom depth and 4-m spacing in height above bottom. In this way, the different sections could be quantitatively compared on the same grid. In the following results, the geographic velocity sections have been transformed back into the traditional cross-stream versus depth coordinate system after calculations were complete. In the stream coordinate system, the origin of the coordinate axes is variable, changing based on the position of the core of the jet (Fig. 5a). The core has been identified in each section by the maximum transport per unit width over the upper 50 m of the water column. To facilitate quantitative comparisons, the individual velocity sections were gridded onto a standard grid with 2-km spacing in the cross-stream direction and 4-m spacing in the vertical. One of the artifacts of the stream coordinate system is that the data density decreases near the edges of the common grid. A threshold was set so that only the portion of the domain containing at least six of the seven velocity realizations is to be considered in the calculations to follow.

### 3. Mean jet structure

Over the 2-yr survey period, the jet remained close to the shelf break (Fig. 6). With one exception, the core of the current was located between the 100-m isobath and the true shelf break at 180 m. This agrees with Linder and Gawarkiewicz (1998), who report a climatological jet position in this area near the 125-m isobath. The jet axis meandered over a lateral range of 30 km, consistent with the range 10–20 km reported by Houghton et al. (1988) for the position of the foot of the shelfbreak property front over a 6-month period. The jet's direction fluctuated between  $245^\circ$  and  $308^\circ$  true (between  $4^\circ$  and  $67^\circ$  off the perpendicular to the survey line), but on average it flowed parallel to the local isobaths (Fig. 6). The jet's width (based on half the core velocity; Linder and Gawarkiewicz 1998) was  $25 \pm 6$  km where the uncertainty represents the standard error.

#### a. Mean jet in geographic coordinates

The seven nonsummer velocity sections have been averaged in the geographic coordinate system and the resulting mean shelfbreak jet is shown in Fig. 7. The

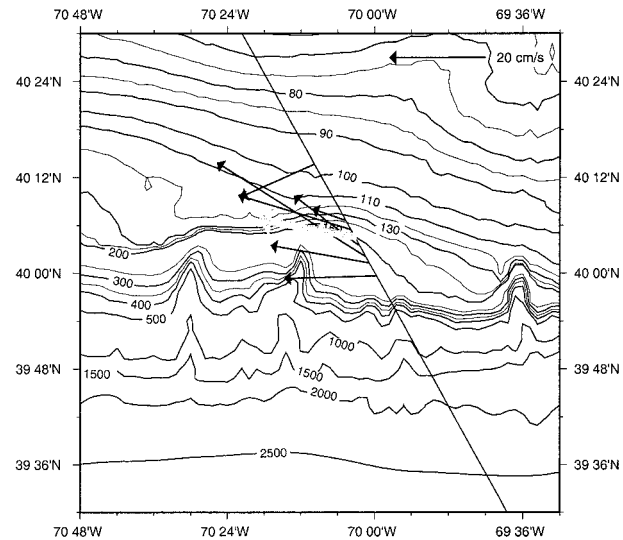


FIG. 6. The position, velocity, and orientation of the jet core for the collection of shipboard surveys (black vectors). The mean jet position and orientation is denoted by the thicker gray vector.

geographic mean shelfbreak jet is broader than the majority of the individual jet realizations, a result of the smoothing due to the nonstationarity of the shelfbreak jet (Fig. 7a). Despite the averaging process, near-surface velocities within the core of the mean jet exceed  $0.30 \text{ m s}^{-1}$ . The alongstream jet axis tilts onshore with depth, approaching the bottom with velocities exceeding  $0.10 \text{ m s}^{-1}$ . The effect of the lateral meandering of the shelfbreak jet is evident in the reduced horizontal velocity gradients relative to the individual sections and is illustrated by the distribution of the standard error of alongstream velocities (Fig. 8a). The variability about the alongstream mean is maximized along the cyclonic (seaward) edge of the shelfbreak jet and near the bottom at the base of the mean alongstream jet core. The cause of the near-bottom variability, which was unexpected, is discussed in section 4. The cross-stream component of the geographic mean jet indicates that there is convergent flow near the surface within the core of the current (Fig. 7b). However, the standard error of the cross-stream velocity field over the remainder of the water column (Fig. 8b) is approximately equal to the mean cross-stream velocity within the jet core (Fig. 7b), indicating that the average cross-stream section in geographic coordinates is only marginally significant.

#### b. Mean jet in streamwise coordinates

When viewed in the streamwise coordinate frame the mean shelfbreak jet is more robust and its secondary circulation is more organized, owing to the fact that a significant amount of variability has been removed by working in stream coordinates. By combining the individual velocity sections in such a manner, we have minimized the variability associated with the meandering of

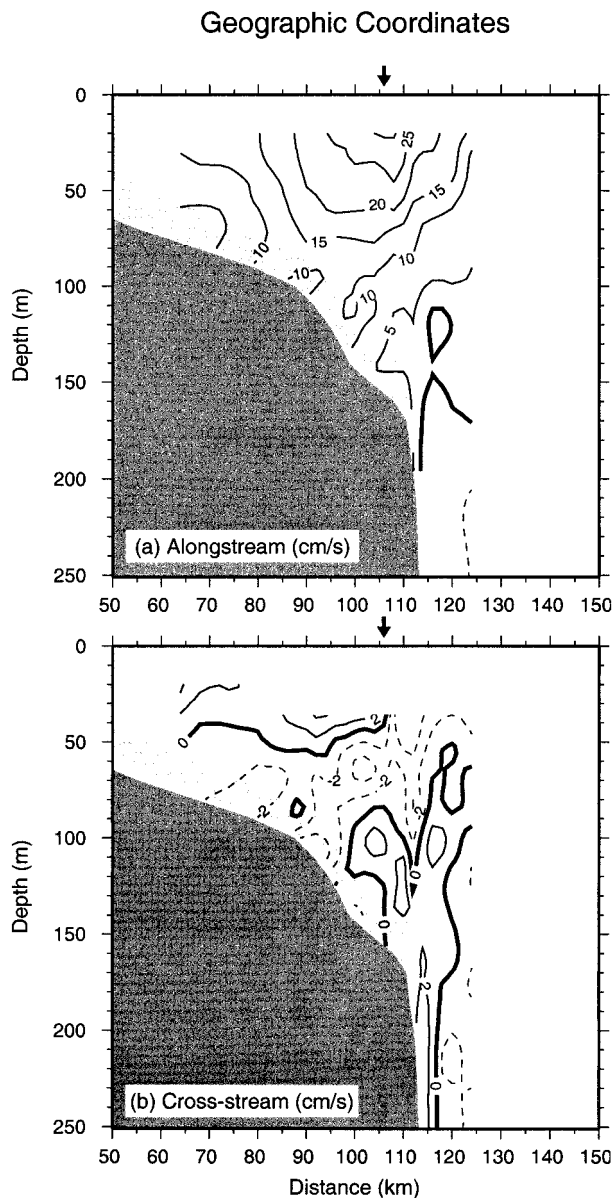


FIG. 7. The mean jet calculated in geographic coordinates for the (a) alongstream and (b) cross-stream components of the flow ( $\text{cm s}^{-1}$ ). The solid contours represent (a) equatorward flow and (b) offshore flow. The shaded region near the bottom corresponds to the extrapolated region in Fig. 3. The arrow denotes the position of the alongstream jet core.

the jet and are left with a highly resolved description of the jet's mean structure (Fig. 9). Without the smoothing that is a consequence of averaging in the geographic coordinate system, the mean shelfbreak jet is narrower and contains more horizontal and vertical shear than its geographic counterpart (compare Figs. 9 and 7). The alongstream jet extends through the water column with its axis tilting onshore with depth (Fig. 9a). The corresponding mean cross-stream flow (Fig. 9b) reveals a clear pattern of convergence that extends along the tilted axis

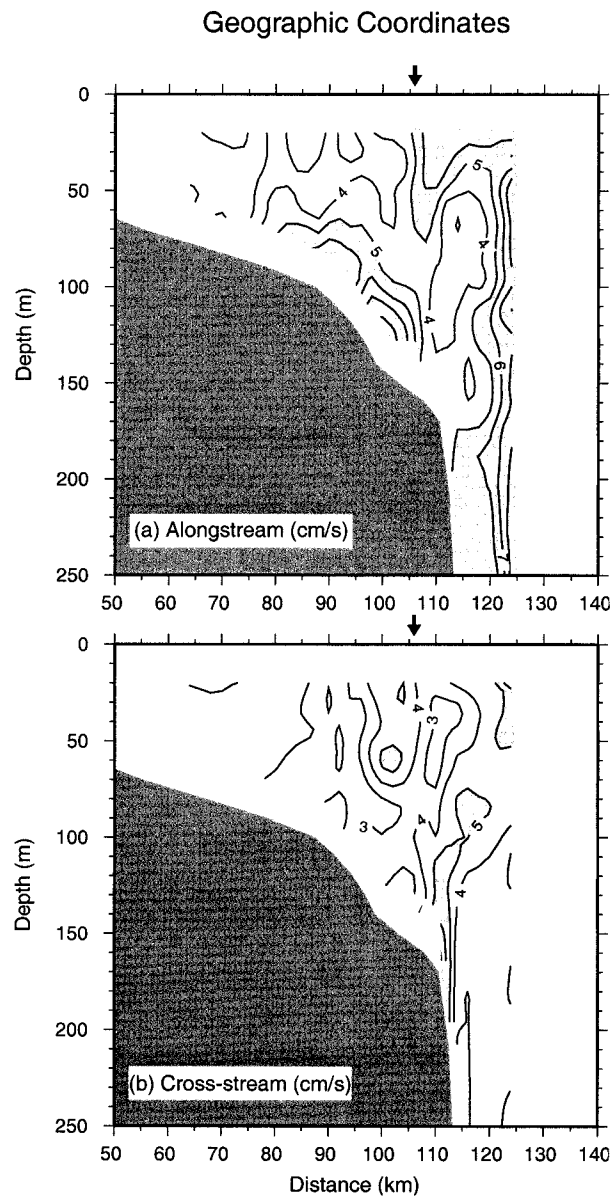


FIG. 8. The standard error ( $\text{cm s}^{-1}$ ) of the mean velocities in Fig. 7. The arrow denotes the position of the alongstream jet core. Standard errors greater than  $0.05 \text{ m s}^{-1}$  are shaded to highlight regions of maximum variability.

of the shelfbreak jet, with enhanced convergence both near the surface and near the bottom. This robust double-celled pattern is not evident in the geographic mean section. Despite that we have minimized the variability associated with the meandering of the jet, it is obvious that some variability remains in the system. In particular, the standard error of the alongstream velocity is largest near the bottom. Note however, that the error velocities are smaller than the mean near-bottom velocities (cf. Figs. 9a and 10a) indicating that the mean section in Fig. 9 provides an accurate description of the mean structure of

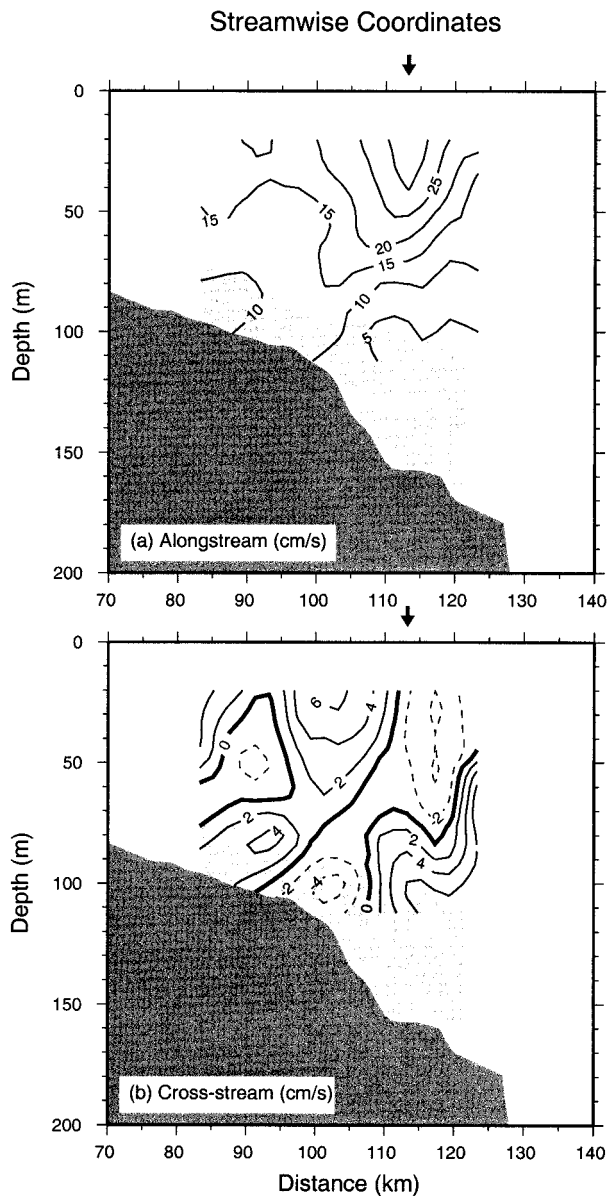


FIG. 9. The mean jet calculated in streamwise coordinates for the (a) alongstream and (b) cross-stream components of the flow. The solid contours represent (a) equatorward flow and (b) offshore flow. The lightly shaded region near the bottom represents the region where less than six (out of the seven) observations contributed to the mean. Velocities in both sections that fall within this region are extrapolated.

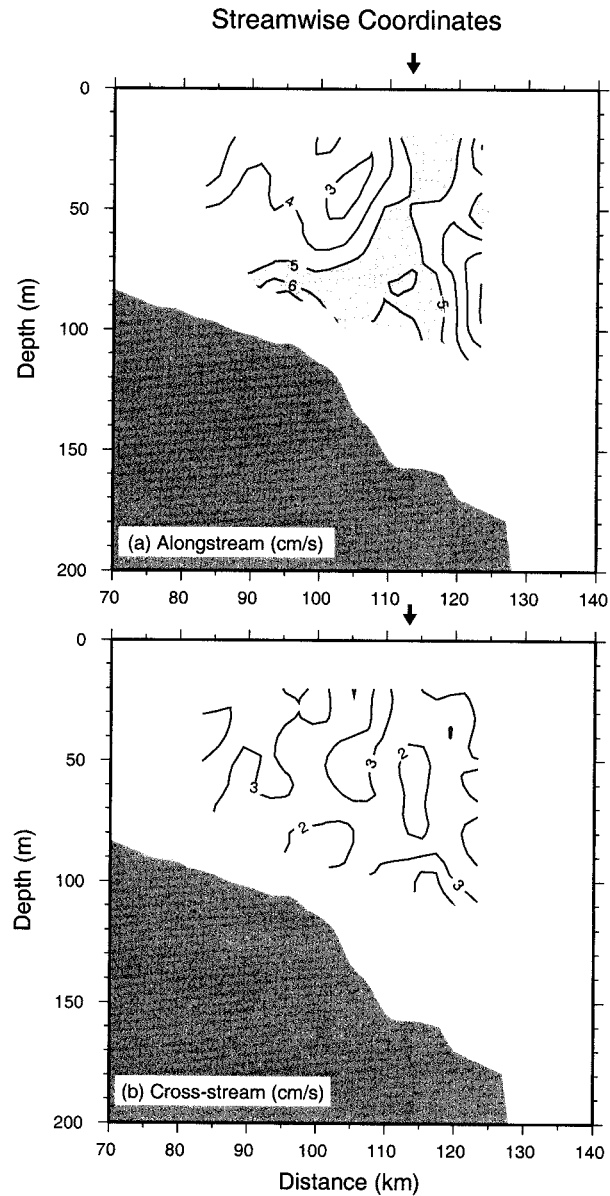


FIG. 10. The standard error ( $\text{cm s}^{-1}$ ) of the mean velocities in Fig. 9. The arrow denotes the position of the alongstream jet core. Standard errors greater than  $0.05 \text{ m s}^{-1}$  are shaded to highlight regions of maximum variability. The blanked region near the bottom corresponds to the extrapolated region in Fig. 9.

the shelfbreak jet throughout the water column. By contrast, the mean cross-stream velocities are only slightly larger than the standard error shown in Fig. 10b, indicating that the secondary circulation, even in stream coordinates, is highly variable. This variability is examined in detail in section 4.

The mean nonsummer shelfbreak jet observed here is surface intensified, in agreement with historical observations. However, unlike previous descriptions, the alongstream flow is not confined to the near-surface lay-

er. Rather, mean alongstream velocities exceed  $0.10 \text{ m s}^{-1}$  near the bottom of the jet axis, located approximately 20 km inshore of the maximum surface velocities. Interestingly, the near-bottom position of the jet core coincides with a “mini-shelf break” located near the 105-m isobath, approximately 25 km inshore of the true shelf break (Fig. 9). This is also true for several of the individual velocity sections and for the position of the bottom intersection of the mean shelfbreak density front (as determined from a smaller number of sections), sug-

gesting that the mini-shelf break may be dynamically important to the circulation in this region.

Due in part to the significant westward flow near the bottom, the mean jet transports a surprisingly large amount of fluid equatorward. Here, the equatorward transport of the jet has been computed over a depth-dependent lateral  $e$ -folding width in order to accommodate the tilted axis of the jet. The transport calculation excludes the velocities within the extrapolated region near the bottom (shaded region in Fig. 9). Further, our transport estimate may be considered a lower bound on the westward transport of the mean jet since it does not include the westward flow within the upper 20 m of the water column where velocity data were not available. The resultant mean transport,  $0.46 \pm 0.32$  Sv, is nearly a factor of 2 larger than previous estimates (Linder and Gawarkiewicz 1998).<sup>3</sup> The variability about this mean, however, is quite large. Taking this into account, our transport estimate is within historical ranges, falling between 0.2 and 0.38 Sv (Beardsley et al. 1985; Linder and Gawarkiewicz 1998). We note that this mean transport, computed in streamwise coordinates, is comparable to the average transport of the collection of individual jet occupations. It should also be noted that most of the earlier transport estimates were based on either geostrophic velocity sections derived from hydrography, which have referencing ambiguities (Linder and Gawarkiewicz 1998), or on direct velocity observations from current meter arrays that were unable to resolve the jet (Beardsley et al. 1985).

### c. Dynamics of the mean jet

The width of the mean jet is approximately 25 km, with maximum lateral velocity gradients located on the cyclonic (offshore) side of the jet (Fig. 11). This is consistent with previous observations of the instantaneous and climatological shelfbreak jet (Gawarkiewicz et al. 2001; Linder and Gawarkiewicz 1998). With the single repeat survey line, we are unable to estimate the component of relative vorticity corresponding to  $\partial v/\partial x$ . However, direct estimates of this term from observations immediately downstream of our location during the same time period indicate that this component is less than 10% of  $\partial u/\partial y$  in the shelfbreak jet (G. Gawarkiewicz 2000, personal communication). The Rossby number of the mean jet, thus defined as  $(\partial u/\partial y)/f$ , peaks at 0.2 implying that the alongstream flow is nearly linear. It is difficult to determine whether the mean jet shown in Fig. 9 is in thermal wind balance because coincident hydrographic data were collected during only four of the seven velocity surveys (Table 1). However, the mean alongstream jet as calculated from this smaller subset of ADCP occupations is in geostrophic balance with the hydrographic structure of the mean front, leading us to con-

<sup>3</sup> Extrapolating over the upper 20 m of the water column, the transport of the jet increases to  $0.63 \pm 0.39$  Sv.

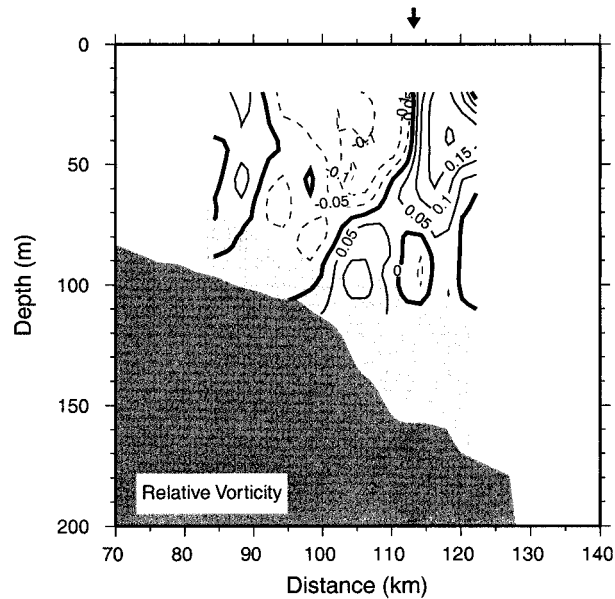


FIG. 11. The cross-stream component of the relative vorticity ( $\partial u/\partial y$ ) scaled by the Coriolis parameter for the mean shelfbreak jet shown in Fig. 9. The solid contours denote cyclonic shear ( $\partial u/\partial y > 0$ ). The arrow denotes the position of the alongstream jet core.

clude that the average jet in Fig. 9 is, to first order, geostrophic.

The shelfbreak jet has been described in the historical literature as a “leaky” coastal current that loses transport as it flows equatorward through the MAB (Loder et al. 1998). However, the mean jet in Fig. 9 is convergent throughout the water column, in contrast to the divergent pattern suggested by large-scale transport estimates. This apparent contradiction is likely due to the fact that the jet, which occasionally extends all the way to the bottom along our survey line, is responding to local bathymetry that is convergent near  $70^\circ\text{W}$ . For instance, Pickart (2000) demonstrated that the cross-stream convergence required by the local isobath configuration, under the constraint of alongshelf continuity of transport, accounts for much of the observed cross-stream convergence in a single jet crossing. Figure 12 shows the cross-stream convergence ( $\partial v/\partial y$ ) calculated from the mean jet in Fig. 9b. The convergent flow is centered along the tilted axis of the alongstream jet with maximum convergence occurring slightly inshore of the jet core. The cross-stream convergence is enhanced near the surface (20 m) and near the bottom, with amplitudes of  $1.3 \times 10^{-5}$  and  $1.0 \times 10^{-5} \text{ s}^{-1}$ , respectively. Note that these two convergent cells are separated by a region of minimum convergence near 70 m.

We now investigate the mass balance in this system using a simple one-dimensional model representing the convergent flow observed at the core of the jet. For simplicity we ignore the shoreward tilt of the jet axis and consider that the profile of  $\partial v/\partial y$ , measured along the axis of the jet in Fig. 12, is vertically aligned. We

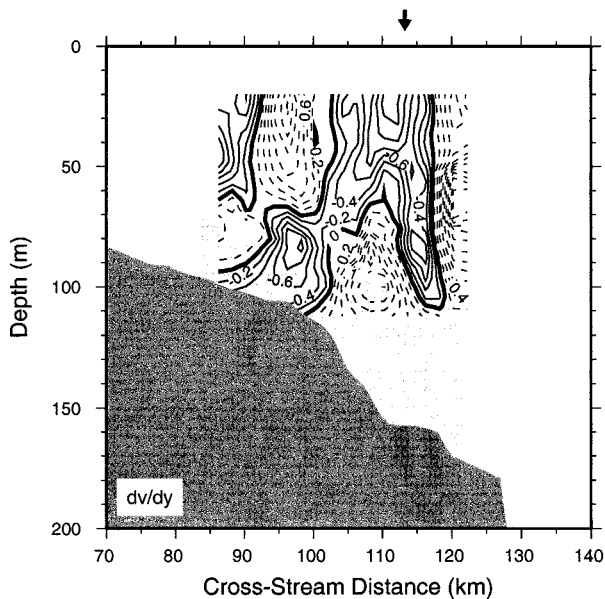


FIG. 12. The cross-stream component of the divergence ( $\partial v/\partial y$ ) ( $\times 10^{-5} \text{ s}^{-1}$ ) for the mean shelfbreak jet shown in Fig. 9. The solid contours denote convergent flow ( $\partial v/\partial y < 0$ ). The arrow denotes the position of the alongstream jet core.

further simplify by assuming that  $\partial u/\partial x$  is independent of depth, a reasonable assumption since we are hypothesizing that the jet responds to the locally convergent topography during a period when the stratification is relatively weak (fall/winter). We are justified in considering this single-layer response based on the arguments of Pickart et al. (1999b), who showed that the penetration height of the jet, defined as  $H = fL/N$  where  $L$  is the width of the jet,  $f$  is the Coriolis parameter, and  $N$  is the buoyancy frequency during winter, is greater than the water depth within the vicinity of the shelfbreak jet. The vertical velocity is taken to be zero at both the bottom and top of our one-dimensional jet. In general, vertical velocities at the bottom are driven by 1) Ekman pumping in the bottom boundary layer, which in this case is predominantly driven by the cross-stream gradient in the alongstream jet velocity,  $\partial u/\partial y$  (since  $\partial v/\partial x$  is comparatively small,  $\leq 10\%$ , as discussed earlier), and by 2) cross-stream flow ( $v$ ) over the sloping topography (e.g., see Pickart 2000). We are confining our one-dimensional model to the axis of the mean jet, where both  $\partial u/\partial y$  (Fig. 11) and  $v$  (Fig. 9b) are identically zero. Taking (the depth independent)  $\partial u/\partial x$  as an unknown, we integrate the continuity equation from the surface to the bottom and vice versa in an iterative fashion, objectively searching for a value of  $\partial u/\partial x$  that causes the vertical velocity to vanish at both the top and bottom boundaries, thereby balancing mass in the interior. We find that the vertical velocity is so minimized at the surface and bottom for  $\partial u/\partial x = 0.9 \times 10^{-5} \text{ s}^{-1}$ . Reassuringly, taking a jet speed of  $0.25 \text{ m s}^{-1}$  and using the observed topographic convergence of the 100 and

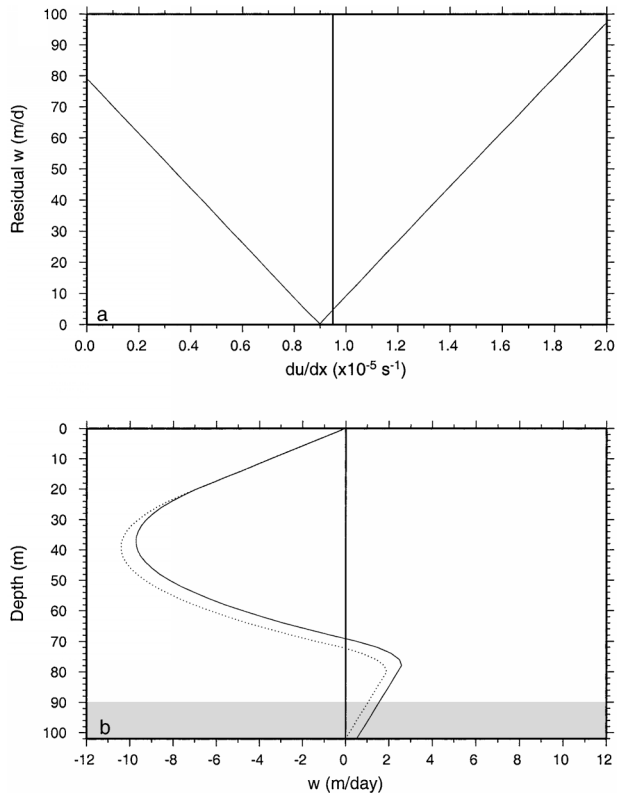


FIG. 13. (a) The residual vertical velocity at the top and bottom boundaries (relative to zero) as a function of the alongstream divergence  $\partial u/\partial x$ . The residual  $w$  is defined as the vertical velocity at the surface when integrating upward, averaged with the velocity at the bottom when integrating downward. The heavy vertical line marks the estimate of the observed  $\partial u/\partial x$ , based on the convergence of the 100-m and 170-m isobaths and assuming a jet speed of  $u = 0.25 \text{ m s}^{-1}$ . (b) The profile of vertical velocity for the one-dimensional jet based on  $\partial u/\partial x = 0.9 \times 10^{-5} \text{ s}^{-1}$ . The solid line results from the integration of the continuity equation originating at the surface and the dotted line results from the integration originating at the bottom. The shaded region is where  $\partial v/\partial y$  is based on extrapolated velocities (Fig. 12).

170 m isobaths where the mean jet is centered, we come up with an estimate for  $\partial u/\partial x$  of  $0.95 \times 10^{-5} \text{ s}^{-1}$ , nearly identical to the objectively determined convergence required to balance mass in the one-dimensional model (Fig. 13a). Thus to leading order, our mean jet balances mass in response to the local convergence of the isobaths. By comparison, the divergence expected due to the larger scale alongstream transport changes [based on transport estimates by Loder et al. (1998) west of the Grand Banks] is only on the order of  $0.01 \times 10^{-5} \text{ s}^{-1}$ , two orders of magnitude less than the convergence forced here by the local isobath configuration. Therefore, it is probable that in locations where the topography is convergent and when the jet extends to the bottom, the resultant convergent flow pattern will dominate over the divergence expected due to the large-scale loss of transport by the jet.

Interestingly, the jet's cross-stream flow (presumably

in response to the convergent topography) is not uniform with depth. Instead it is intensified near both the surface and the bottom, with weakly convergent flow at mid-depth. Our simple model suggests that much of the convergent fluid near the surface and bottom directly feeds the downstream acceleration of the jet, while the imbalance results in downwelling near the surface and upwelling near the bottom (Fig. 13b). At middepth,  $\partial w/\partial z$  must balance the alongstream acceleration of the jet as  $\partial v/\partial y$  is not sufficient to balance the downstream acceleration. As a result,  $w$  passes through zero and the downwelled/upwelled water turns downstream, closing the secondary cell (Fig. 13b). One wonders why the jet's response to the convergent topography might be nonuniform in the vertical and what drives the downwelling/upwelling cells. Near-surface downwelling cells have been inferred from observations in association with both open ocean fronts (Pollard and Regier 1992) and more recently in the shelfbreak jet (Barth et al. 1998; Gawarkiewicz et al. 2001). Pollard and Regier (1992) demonstrated that vertical velocities result from the requirement that potential vorticity is conserved within a confluent flow in the vicinity of the frontal jet. Specifically, water parcels are transported by the confluent flow (in Pollard and Regier's case by transient baroclinic eddies) into regions of increasing (or decreasing) relative vorticity, while conservation of potential vorticity requires that the parcels adjust their thickness to compensate, resulting in the vertical velocities. For a simple jet this implies that there will be downwelling to the right and upwelling to the left of the jet axis, looking upstream.

Formally, the details of the ageostrophic circulation can be described by applying the quasigeostrophic approximation to the nonlinear equations of motion. Following Gill (1982):

$$f_o u_a = -\beta y u_g - \left( \frac{\partial v_g}{\partial t} + u_g \frac{\partial v_g}{\partial x} + v_g \frac{\partial v_g}{\partial y} \right) \quad (1)$$

$$f_o v_a = -\beta y v_g + \left( \frac{\partial u_g}{\partial t} + u_g \frac{\partial u_g}{\partial x} + v_g \frac{\partial u_g}{\partial y} \right), \quad (2)$$

(a)                      (b)                      . . . . . (c) . . . . .

where  $\beta$  is the meridional gradient of the Coriolis parameter,  $(u_a, v_a)$  represent the ageostrophic component of the flow, and  $(u_g, v_g)$  denote the geostrophic part of the flow so that  $(u, v) = (u_g, v_g) + (u_a, v_a)$ . There are three components to the ageostrophic flow: (a) the  $\beta$  term results in ageostrophic flow driven by the advection of planetary vorticity, (b) the time-dependence of the geostrophic flow, and (c) the nonlinear advection, resulting in ageostrophic flow driven by the advection of relative vorticity. Pollard and Regier (1992) considered terms (b) and (c) in their diagnosis of the ageostrophic flow near an open ocean front. In their case, the confluent flow was associated with transient eddies in the vicinity of the front.

We have shown that the convergent topography in this region likely results in the downstream acceleration of the mean shelfbreak jet, driving a large portion of the convergent mean cross-stream flow in Fig. 9b. One wonders if this convergence could have the same effect as the confluent flow of the transient eddies examined by Pollard and Regier (1992), setting up an ageostrophic secondary circulation. The mean flow in Fig. 9 is a zonal jet and is presumably in steady-state balance, therefore the first two terms on the right-hand side in Eqs. (1) and (2) do not contribute to ageostrophic flow. Because we are interested in the secondary circulation in the cross-stream plane, we concentrate on Eq. (2), which reduces to

$$v_a = \frac{1}{f_o} \left[ u_g \frac{\partial u_g}{\partial x} + v_g \frac{\partial u_g}{\partial y} \right]. \quad (3)$$

This assumes that the observed alongstream flow,  $u$ , is primarily geostrophic. This is reasonable based on the small Rossby number of the mean jet (Pickart et al. 1999b) and based on the thermal wind agreement discussed above. Therefore,  $u_g$  is taken as the observed mean alongstream velocity. The divergence term,  $\partial u_g/\partial x$ , is taken to be  $0.9 \times 10^{-5} \text{ s}^{-1}$  as predicted by the one-dimensional model and confirmed by considering the acceleration of the jet confined between the 100-m and 170-m isobaths. The vorticity term,  $\partial u_g/\partial y$ , is taken from Fig. 11. Finally,  $v_g$  is the geostrophic part of the mean cross-stream velocity (as yet undetermined). We assume that  $v_g$  is driven by the converging isobaths, and therefore it satisfies  $\partial v_g/\partial y = -\partial u_g/\partial x = -0.9 \times 10^{-5} \text{ s}^{-1}$ . Thus we can determine  $v_g$  up to a constant of integration,  $v_g = -(\partial u_g/\partial x)y + v_{g_o}$ . Depending on the choice of  $v_{g_o}$ , we produce different magnitudes of  $v_a$  according to Eq. (3). To determine the optimal choice of  $v_{g_o}$ , we used the constraint  $v_{\text{obs}} = v_g + v_a$ , where  $v_{\text{obs}}$  is the mean cross-stream velocity shown in Fig. 9b. Note that in general this constraint cannot be satisfied everywhere (specifically it is not possible to satisfy this at the edges of the jet where the value of  $v_g$  increases without bound, see Fig. 14b). For this reason, we confined ourselves to the central portion of the jet and determined the value of  $v_{g_o}$ , which minimized the rms difference between  $v_{\text{obs}}$  and  $(v_g + v_a)$ .

We evaluate Eq. (3) at each depth but vertically average the resulting values of  $v_g$  and  $v_a$  to simplify their comparison in Fig. 14. It is important to note that each of the terms contributing to the calculation of the ageostrophic flow in Eq. (3) is based on a variable in which we have confidence. For instance, the calculations were limited to the upper 50 m where the mean alongstream velocity is most robust (compare Figs. 9a and 10a) and all other terms are based on our estimate for the alongstream acceleration of the jet in response to the converging isobaths. Although the mean cross-stream velocity field in Fig. 9b is less robust, this was used only to constrain the value of the integration constant  $v_{g_o}$ .

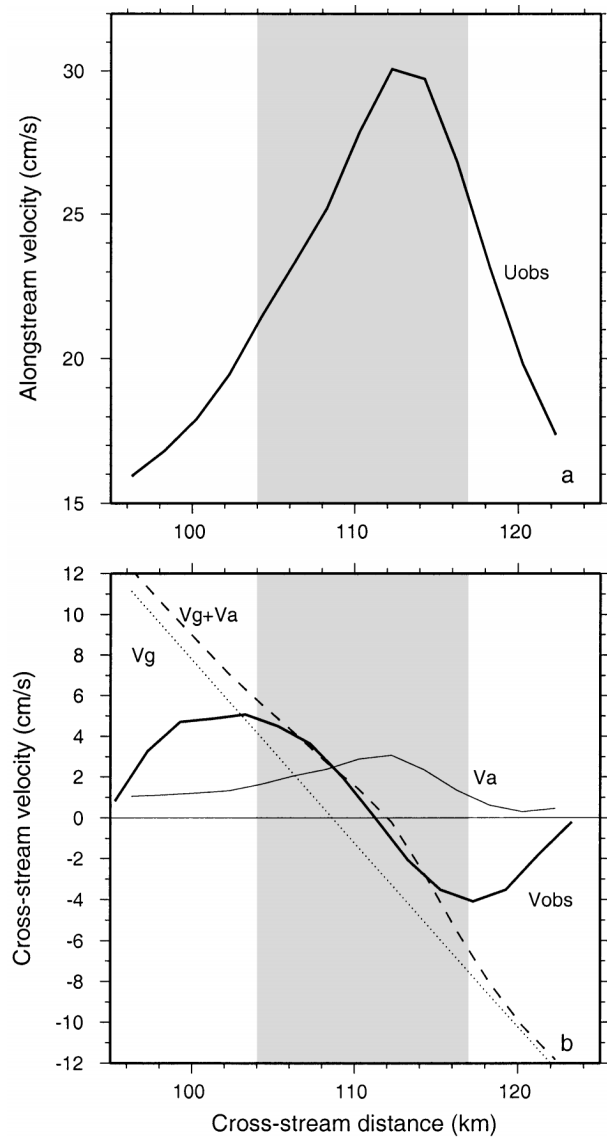


FIG. 14. (a) Vertically averaged (20–50 m) alongstream velocity ( $u_{obs}$ ) from Fig. 9a. (b) Comparison of the vertically averaged (20–50 m) observed cross-stream velocity ( $v_{obs}$ ) the geostrophic component of the cross-stream velocity ( $v_g$ ), the calculated ageostrophic cross-stream velocity ( $v_a$ ), and the sum ( $v_g + v_a$ ). The shaded region, corresponding to the central portion of the jet, indicates the region over which  $v_g$  was optimized (see text).

Note that the cross-stream gradient in  $v_a$  (which is the quantity that determines the distribution of vertical velocity) is independent of this integration constant. Hence, we believe that  $v_a$  so calculated represents an accurate measure of the ageostrophic secondary circulation of the mean jet.

The vertical section of ageostrophic flow computed using Eq. (3) is shown in Fig. 15a. The ageostrophic velocity is directed offshore over the majority of the section with maximum flow located just inshore of the mean jet core. The divergence of the ageostrophic ve-

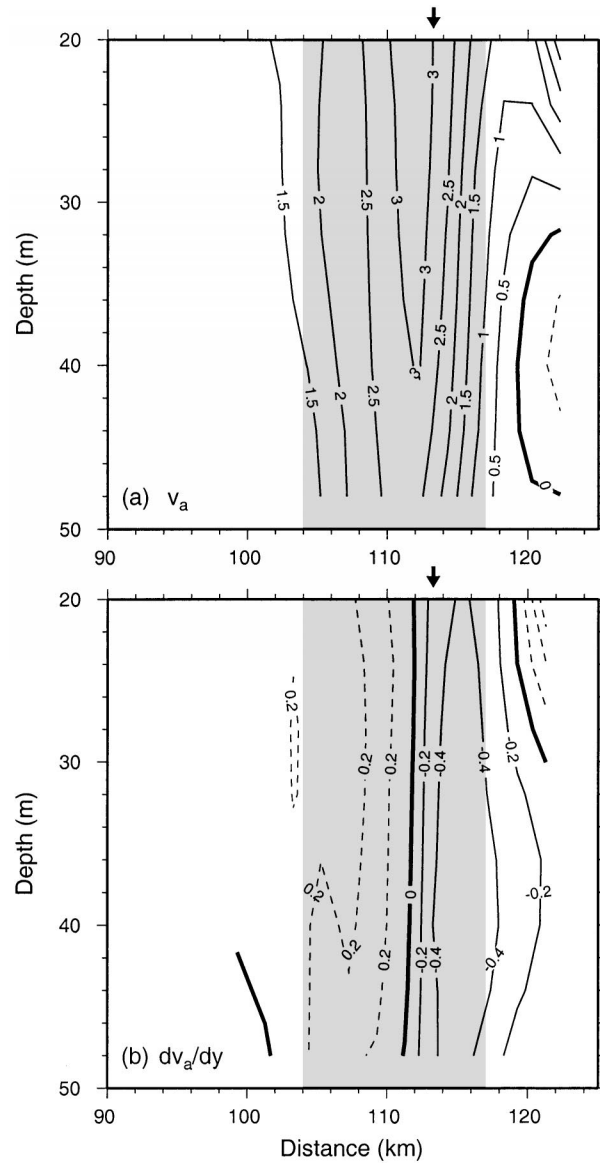


FIG. 15. (a) Ageostrophic velocity calculated over the upper 50 m of the water column. Solid contours denote offshore flow in  $\text{cm s}^{-1}$ . (b) Divergence of ageostrophic velocity in (a). Solid contours represent convergent flow. The arrows denote the location of the mean jet core as shown in Fig. 9. The shaded region denotes the central portion of the jet.

locity ( $\partial v_a / \partial y$ ) is shown in Fig. 15b. Interestingly, the ageostrophic cell is not symmetric about the mean core of the jet. Instead, the magnitude of the convergence on the seaward side is twice that of the divergence on the shoreward side. This asymmetry in the ageostrophic flow is a direct consequence of the asymmetry of the jet: as mentioned earlier, the lateral shear is greater on the cyclonic side (Fig. 11). Although the maximum convergence is located offshore of the jet core, the region of convergent flow extends inshore of the core with magnitudes of  $0.3 \times 10^{-5} \text{ s}^{-1}$  at the jet core. As a

consistency check, we can compare this value to the residual computed between the observed cross-stream convergence, from Fig. 12, and the geostrophic convergence predicted based on the downstream convergence of the isobaths in this region,  $\partial v_{\text{obs}}/\partial y - \partial v_g/\partial y$ . The residual,  $0.4 \times 10^{-5} \text{ s}^{-1}$  at the jet core, is in good agreement with the ageostrophic convergence in Fig. 15b.

This analysis suggests that the downstream acceleration of the mean jet, in response to the converging isobaths, does indeed modify the momentum balance so that a secondary ageostrophic circulation results. In this way, the convergent topography induces a confluent flow similar to that set up by the transient eddies examined by Pollard and Regier (1992), which resulted in an ageostrophic circulation cell in their open-ocean front case. The ageostrophic circulation at the shelf break deduced here is an asymmetric cell with convergence and downwelling at the jet core, extending offshore, and weaker divergence and upwelling inshore of the jet core. For computational purposes, our calculation is limited to the upper 50 m where the alongstream mean velocity field is significantly greater than the standard error, and hence the results are robust. Obviously, if the topography is responsible for modifying the momentum balance as we have suggested, we would not expect the ageostrophic circulation to be limited to the upper water column. However, both the magnitude of the mean alongstream flow and its lateral gradients decrease near the bottom indicating that the ageostrophic flow should also decrease.

We note that the ageostrophic circulation determined here has been diagnosed in an inviscid framework, although it has been shown that frictional effects play an important role in the maintenance of the shelfbreak front (Gawarkiewicz and Chapman 1992; Chapman and Lentz 1994). In the presence of friction, an Ekman layer is established in the bottom boundary layer, which drives upwelling within the frontal zone (Chapman and Lentz 1994; Pickart 2000). This upwelling occurs a bit inshore of the foot of the front and is responsible for the initial detachment of the bottom boundary layer at the base of the shelfbreak front (Chapman and Lentz 1994). The dye release experiments of Houghton (1997) and Houghton and Visbeck (1998) were the first to directly observe this detachment process in the shelfbreak jet. Although we do not resolve the bottom boundary layer with the ADCP velocity sections, it has been demonstrated that strong cross-stream convergence at depth (above the bottom boundary layer) can lead to upwelling, which enhances the upward advection of the detached bottom boundary layer (Pickart 2000). This is consistent with the enhanced near-bottom convergence seen in Fig. 9b.

#### 4. Jet variability

The distribution of the standard error in stream coordinates reflects the variability associated with the

change in the shape, vertical orientation, and intensity of the shelfbreak jet (Fig. 10). The variability about the alongstream mean jet in stream coordinates is largest near the bottom, where the jet axis encounters the mini-shelf break. To investigate this variability further, we applied an empirical orthogonal function (EOF) analysis to the ensemble of velocity sections in stream coordinates. The EOF technique computes the eigenvalues and eigenfunctions of the velocity covariance (or correlation) matrix to objectively identify the dominant modes of variability associated with the collection of velocity sections. As in the mean calculation, only the portion of the domain containing at least six of the seven velocity realizations is considered in the EOF analysis. Hence, this EOF is similar to the sparse EOF invoked by Pickart et al. (1999a). Admittedly we are working with a very small number of velocity sections for an EOF analysis, but the well-behaved nature of the results and the significance of the dominant modes lends credibility to the present application of the method. With so few sections, it is possible for a single realization to dominate the EOF structure if the magnitude of the signal in question is significantly larger and more anomalous than the surrounding velocities in space and time. Indeed, the presence of a nearby Gulf Stream ring during one of our jet crossings resulted in anomalously strong poleward flow over the edge of the continental slope, immediately seaward of the shelfbreak jet. This signal unduly influenced the results from our initial EOF, by focusing the structure of the dominant modes entirely over the slope region and dominating the principal component amplitude time series. As this was the only section in our collection that was obviously impacted by a Gulf Stream ring, we objectively removed the anomalous poleward slope water velocities from this section using the coincident temperature and salinity data to define the slope water boundary, leaving the velocities within the shelfbreak jet untouched. An EOF analysis was then performed on the two components of velocity (along- and cross-stream) separately, followed by a bivariate EOF on  $u$  and  $v$  simultaneously. The results of the two calculations were largely similar, indicating that the variability described by the EOFs for the along- and cross-stream fields are directly related. The results from the uncoupled calculation are presented here, as they are a bit cleaner.

The first EOF describes the dominant mode of variability, containing four times (twice) the variance of the next dominant mode in the alongstream (cross-stream) case. The first mode amplitude time series and vertical structure are presented in Fig. 16. The amplitude time series is normalized so that the vertical structure of the EOF represents the maximum dimensional value of the mode. The vertical structure of the first EOF suggests acceleration/deceleration of the alongstream velocity across the entire section, while the cross-stream velocity varies out of phase inshore and

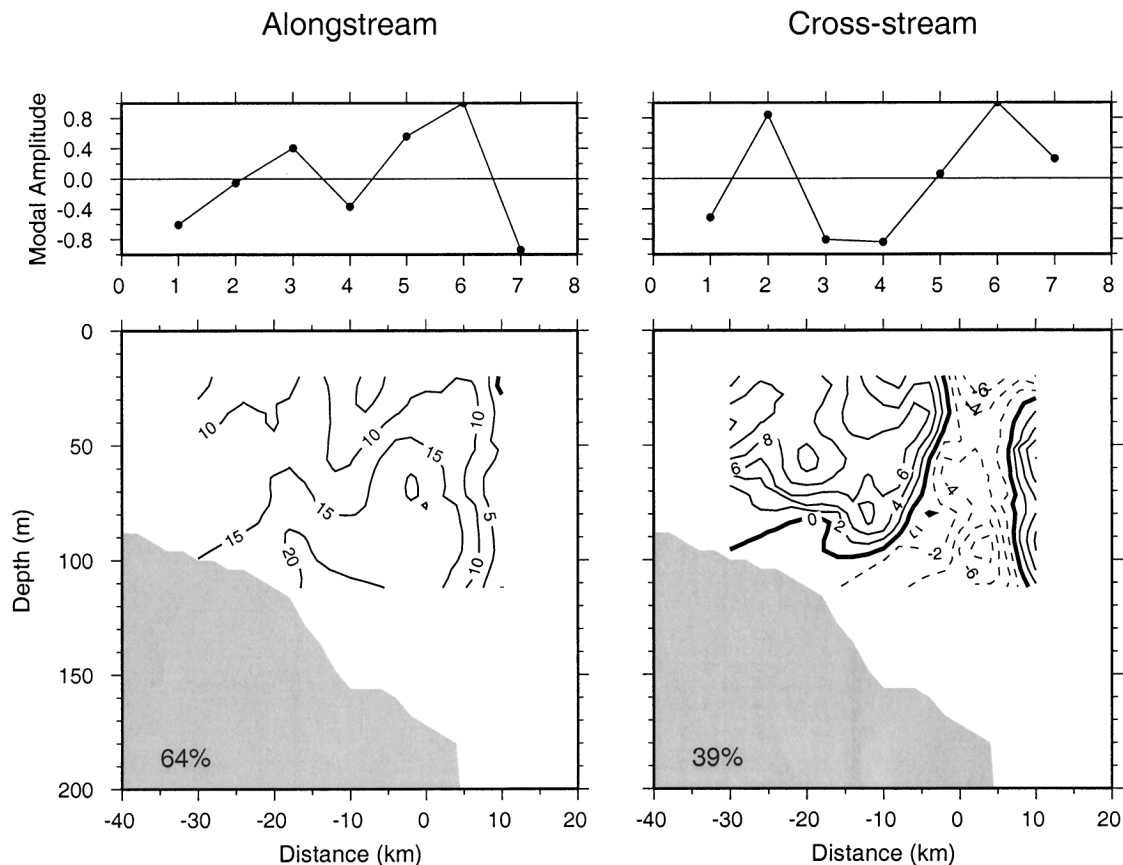


FIG. 16. The vertical structure of the dominant EOF mode as calculated for the alongstream (lower left) and cross-stream (lower right) velocity fields. The percent variance explained by the mode is indicated. The normalized "time series" (upper panels) of the modal amplitudes (the abscissa is labeled based on the shipboard survey numbers from Table 1). The vertical structure fields are dimensional and represent the maximum value of the mode. The mean position of the jet core (not shown) is located at  $x = 0$  km near the surface, corresponding to the origin of the stream coordinate system (Fig. 5).

offshore of the jet axis (Fig. 16). The alongstream variability is maximized within a tongue of relatively high amplitudes extending from the bottom along the axis of the mean jet (Fig. 9a). Because the vertical structure of the alongstream EOF is of the same sign over the entire section, this mode can be interpreted as a "transport mode." By contrast, the cross-stream variability is largely symmetric about the core of the mean jet, although amplitudes are slightly higher on the inshore side. In order to visualize the effect of this variability on the structure of the shelfbreak jet, we have added the mean fields back into the first EOF and compared the structure of the resulting extreme minimum and maximum states (Fig. 17). This suggests that the shelfbreak jet systematically fluctuates between a convergent, bottom-reaching state and a more surface-trapped state with weaker cross-stream velocities. The surface-trapped jet is much broader and weaker than the bottom-reaching jet (as evidenced by the differences in the relative vorticity in Fig. 17) and is associated with a deep alongstream flow reversal (poleward flow) rem-

iniscent of the Chapman and Lentz (1994) model jet. Except for the third realization, the alongstream and cross-stream modal amplitude time series vary in phase with each other (Fig. 16), confirming that these fluctuations are coupled, as the results from our bivariate EOF had already suggested. The third occupation of the shelfbreak jet revealed a jet structure that could be fairly well described by either state in Fig. 17. During this occupation, the jet was convergent and its axis extended to the bottom with an onshore tilt at depth. However, offshore of the deep core of the jet, the alongstream flow reversed. This poleward flow reversal is likely the reason for the disagreement between the alongstream and cross-stream modal amplitudes at this time.

In summary, the dominant mode of variability revealed by the EOF analysis is one in which the shelfbreak jet periodically retracts off the bottom (with weak cross-stream flow) and then extends to the bottom (with strong convergence). The former state seems to be associated with a deep alongstream flow reversal. These

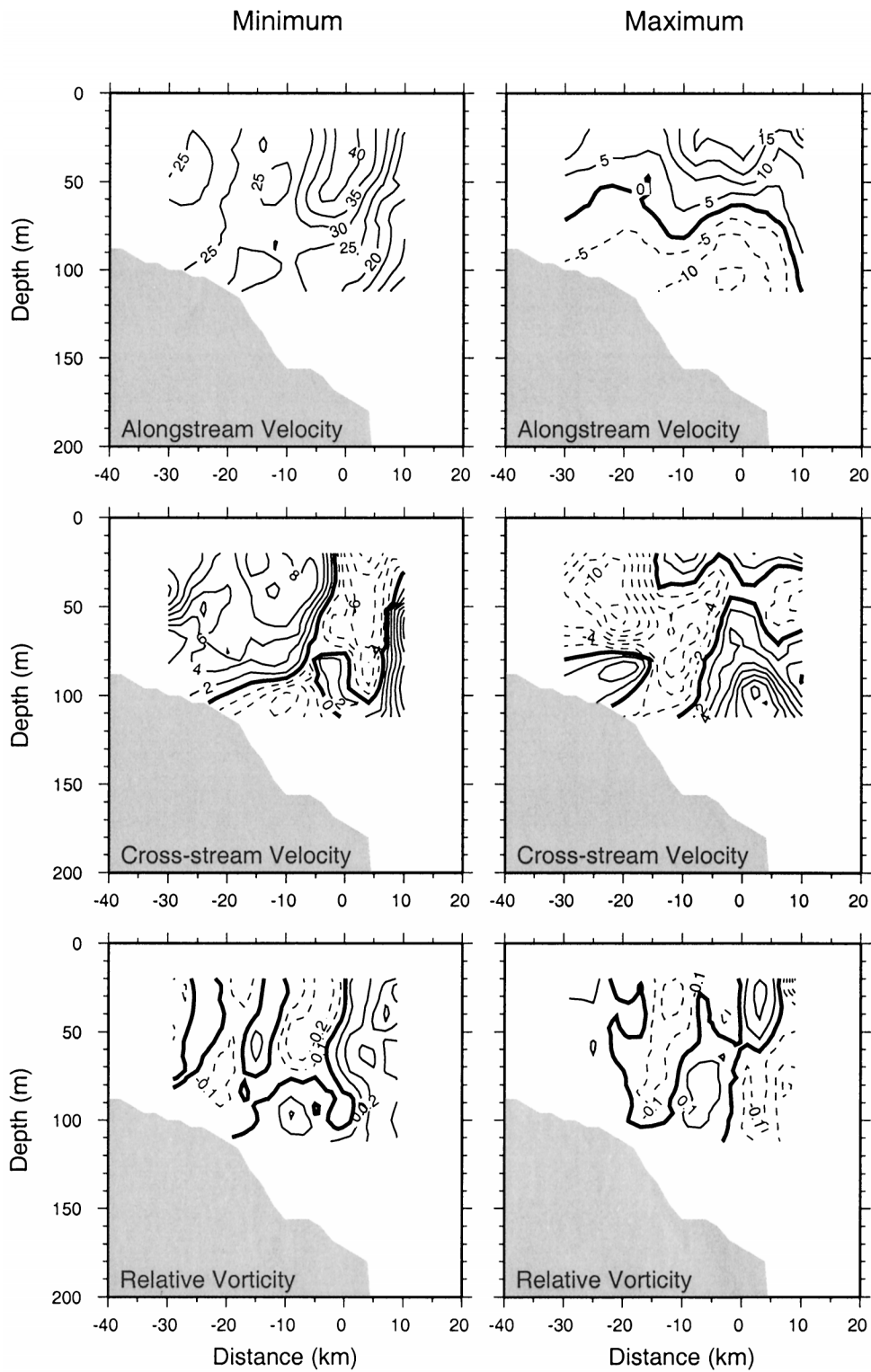


FIG. 17. Minimum (left) and maximum (right) values of the EOF mode shown in Fig. 16 with the mean included. The two lower panels show the relative vorticity ( $\partial u/\partial y$ ) corresponding to the alongstream flow in the top panels, scaled by the Coriolis parameter.

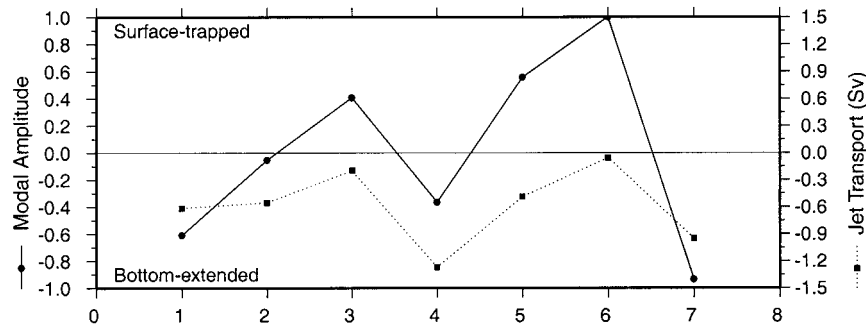


FIG. 18. Comparison of the modal amplitude “time series” (solid line) with the fluctuations in equatorward transport (dotted line). The abscissa is labeled as in Fig. 16.

two states are identifiable in the individual velocity sections, indicating that these patterns are representative of the true variability during the 2-yr survey period. That the jet is strongly convergent in its bottom-reaching state lends credence to the idea that it is responding in part to the locally convergent topography as previously discussed.

#### *Causes of variability*

The fluctuations in the structure of the shelfbreak jet that are described by this EOF have not been seen in previous studies. This is not surprising since it took a collection of high-resolution, direct velocity observations viewed in streamwise coordinates to identify the variability. It is well known that the shelfbreak jet fluctuates in response to various types of forcing. However, little is known about the relative importance of these forcing mechanisms and even less is known about their effect on the detailed structure of the shelfbreak jet. In view of the sensitivity of the jet to these different mechanisms, one wonders why the variability at our survey line seems to be dominated by a single mode. Furthermore, can one unambiguously attribute this observed jet variability to one or several of the possible forcing mechanisms (e.g., winds, internal instabilities, anticyclonic rings)? Although it is beyond the scope of this work to identify the precise causes of the variability described by the first EOF, it is instructive to explore some of the possible candidates.

Lozier and Gawarkiewicz (2001) have demonstrated that cross-shelf meandering of the shelfbreak jet axis is apparently ubiquitous throughout this region, suggesting that perhaps the variability described by the EOF is forced internally by instabilities in the current. However, the fluctuations in the EOF modal amplitude are not correlated with the cross-slope position of the jet core or with its orientation, both of which are indices of the meandering of the jet. Instead, the EOF is interpreted as a transport mode whereby fluctuations in jet structure are significantly correlated with substantial changes (nearly an order of magnitude) in westward transport (Fig. 18). This further suggests that the variability ob-

served here is not simply due to the meandering of the jet.

Perhaps the most dominant external influence on the shelfbreak jet is the circulation in the adjacent slope water. For instance, Gawarkiewicz et al. (2001) observed structural changes in the shelfbreak jet reminiscent of those described here over an alongslope distance of approximately 30 km and over the course of two days. Interestingly, they also observed significant changes in westward transport. They attribute the structural differences to the presence of an anticyclonic eddy that was observed over the upper continental slope. They argue that the onshore (offshore) flow associated with the slope eddy forced alongslope variations in the jet by steepening (flattening) the surface outcrop of the front. In a similar manner, it is possible for this type of near-surface, frontal variability to be forced by synoptic wind events (Houghton et al. 1988). In general, the transport fluctuations that we observe are caused primarily by fluctuations in the near-bottom velocities. For instance, we find no significant correlation between the Rossby numbers calculated for each jet realization and the fluctuations in westward transport. This implies that the fluctuations in transport are not a result of the strengthening (or weakening) of the core jet velocity, which should result in larger (or smaller) Rossby numbers. Instead, it is the width and the penetration depth of the jet that predominantly control the transport fluctuations. Hence, the scenario described by Gawarkiewicz et al. (2001) does not appear to apply to the fluctuations that we observe here.

As previous studies have illustrated, the shelfbreak jet is sensitive to both internal and external influences, making it difficult to identify the relative influence of one forcing mechanism over another. With our limited dataset we are unable to attribute easily the observed variability to any one of the possible forcing mechanisms described above—although, the characteristics of the variability imply that simple meandering alone is not the cause. A much greater ensemble of velocity sections, which are highly resolved in time, will be necessary to definitively determine the nature of the shelfbreak jet variability revealed here.

## 5. Summary

Making use of a collection of shipboard ADCP velocity observations, taken along a section that crosses the shelf break near 70°W, we have produced a highly resolved description of the structure of the shelfbreak jet during the winter and fall in the Middle Atlantic Bight (MAB). Because high frequency tidal and inertial oscillations are easily aliased into such shipboard ADCP velocity observations, a tidal prediction algorithm was developed to successfully predict and minimize the barotropic tide in the individual velocity sections. Further, it was determined that the amplitude of both the baroclinic tide and episodic inertial oscillations was small compared with the signals of the jet in this region. A mean velocity section was computed with respect to a stream wise coordinate system that, by definition, eliminates the differences in position and orientation of the jet's axis between sections. This has resulted in the first-ever, high-resolution mean description of both the primary and secondary structure of the shelfbreak jet in the MAB.

The mean shelfbreak jet constructed as such occupies the full water column with alongstream velocities exceeding  $0.10 \text{ m s}^{-1}$  just above the bottom. Our velocity measurements indicate that the mean jet transports  $0.46 \pm 0.32 \text{ Sv}$  equatorward over 70% of the water depth. By extrapolating over the upper 20 m where velocities are large but ADCP observations are not available, the transport increases to  $0.63 \pm 0.39 \text{ Sv}$ . While the variability in observed transport is large, the measured transport is at the upper limit of historical estimates. The jet's axis is tilted onshore with depth and approaches the bottom near a mini-shelf break, inshore of the true shelf break. The cross-stream flow reveals that the mean jet is convergent along the tilted axis of the current, with enhanced convergence near the surface and the bottom. We have shown that a majority of the convergent flow feeds the downstream acceleration of the mean jet, which is responding to the locally convergent topography in this region. This topographically driven confluent flow modifies the momentum balance so that a secondary ageostrophic circulation results, which we diagnosed using the mean velocity data. The ageostrophic circulation is characterized by an asymmetric cell that is dominated by convergence and downwelling in the upper layer at, and offshore of, the jet core.

An EOF analysis was applied to the ensemble of velocity sections in order to identify the dominant mode of variability associated with the structure of the jet. The jet appears to systematically fluctuate between a bottom-reaching, convergent state (similar to the mean structure) and a more surface-trapped state with weaker, cross-stream velocities. Presumably the shelfbreak jet is responding to the convergent topography when it extends to the bottom. Historical observations have shown that the shelfbreak jet is sensitive to a large number of forcing mechanisms, though it is not clear which mech-

anism is responsible for the systematic variability observed here. As might be expected, the transition between the bottom-reaching and surface-trapped jet is correlated with a significant change in equatorward transport. However, these fluctuations are not coherent with either the cross-shelf jet position or with jet orientation. This evidence suggests that the variability described by the EOF analysis is not simply due to the meandering the jet; further measurements will be necessary to sort this out.

*Acknowledgments.* The authors gratefully acknowledge the many helpful insights offered by Glen Garkiewicz and Mike Spall throughout the course of this work. We are also thankful to Ken Brink and Robert Beardsley for their input during the early stages of this analysis. Discussions with David Chapman resulted in a clearer presentation of this work. This work was supported by Office of Naval Research Contract N00014-98-10046 as part of the Shelfbreak PRIMER Experiment. A. S. was supported by the Postdoctoral Scholar Program at the Woods Hole Oceanographic Institution, with funding provided by the Johnson Foundation.

## APPENDIX

### Barotropic Tidal Correction Scheme

In order to predict the barotropic tide at any given time along the survey line, we constructed a local model based on long-term current measurements taken at moorings deployed along the TOPEX line (Fig. 1). Table A1 lists the positions of the five moorings, together with the water depth and the length of the record. From the data at each mooring we constructed a time series of the barotropic (vertically averaged) component of the flow. The tidal component of the signal can be written as

$$(u, v)(t) = \sum_{i=1, \dots, n} (cu_i, cv_i) \cos(\omega_i t + \phi_i) + (su_i, sv_i) \sin(\omega_i t + \phi_i), \quad (\text{A1})$$

where  $\omega_i$  are the frequencies of the tidal constituents (which are known),  $(cu_i, cv_i)$  and  $(su_i, sv_i)$  the amplitudes, and  $\phi_i$  the phases, which are computed using the Foreman method (Foreman 1978) at each site. Table A2 lists the tidal constituents that have been included in the model for each mooring. This choice of constituents was made according to the following criteria:

- 1) The Raleigh criterion restricts the number of constituents that can be extracted from a signal of finite length,  $T$ . Specifically, if a constituent of frequency  $\omega_i$  is extracted from a signal, then the constituent with frequency  $\omega_j$  can be extracted without aliasing errors if and only if  $|\omega_i - \omega_j|T > 1$ .
- 2) We exclude tidal constituents whose amplitude is smaller than the amount of signal variance not accounted for by the tidal harmonic decomposition.
- 3) The tidal constituents whose ellipses show large var-

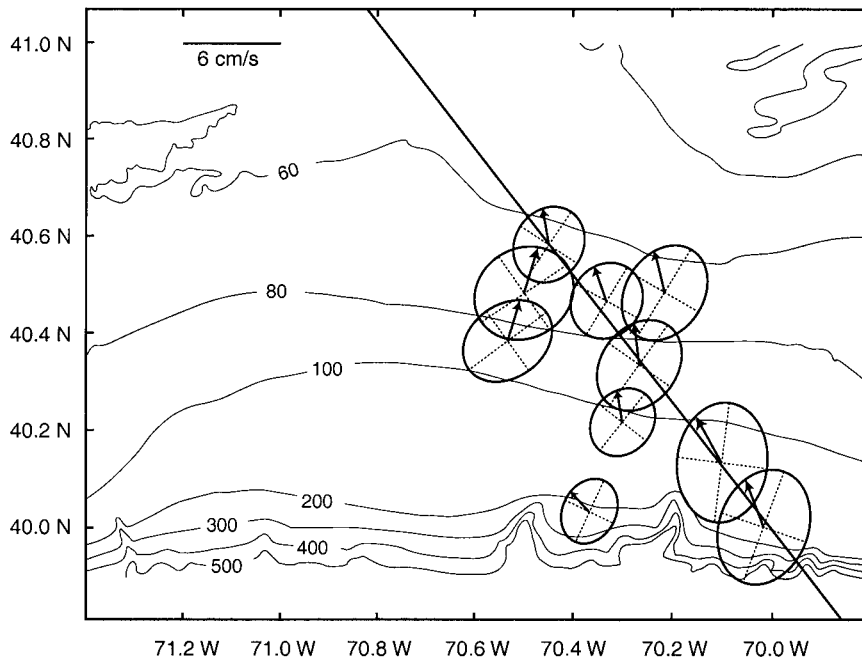


FIG. A1. Tidal ellipses for the  $M_2$  component at each mooring location. The vectors denote the current direction at a given time during the tidal cycle. The solid line denotes the repeat survey line.

TABLE A1. Position and characteristics of the moored velocity observations used in constructing the tidal model. The instruments include upward-facing acoustic Doppler current profilers (ADCP), vector averaging current meters (VACMs), and vector measuring current meters (VMCMs).

Site	Position	Depth (m)	Length (h)	Instrument
PRIMER (deep)	40.000°N, 70.010°W	168	5239	ADCP
PRIMER (shallow)	40.140°N, 70.100°W	125	4879	ADCP
NSFE	40.354°N, 70.268°W	88	1113	VACMs
CMOA	40.475°N, 70.333°W	70	737	VMCMs
CMOI	40.583°N, 70.458°W	64	5373	VMCMs

TABLE A2. Tidal constituents included at each site. The amplitude ( $\text{cm s}^{-1}$ ) of the major (top) and minor (bottom) axes are indicated for each constituent included in the tidal model.

Site	$Q_1$	$O_1$	$\tau_1$	$K_1$	$\phi_1$	$N_2$	$M_2$	$S_2$	$MSN_2$	$M_3$	$MN_4$	$M_4$	$MS_4$
Period (h)	26.87	25.82	25.67	23.93	23.80	12.66	12.42	12.00	11.79	8.28	6.27	6.21	6.21
PRIMER (deep)	0.35 0.24	2.14 1.52	0.28 0.18	3.44 2.65	0.40 0.35	1.51 1.22	7.13 5.36	0.84 0.70	0.49 0.40	0.11 0.04	0.01 0.00	0.24 0.04	0.06 0.03
PRIMER (shallow)	0.39 0.24	2.88 2.11	0.44 0.18	4.31 3.52	0.65 0.06	2.15 1.74	9.89 7.29	1.10 0.83	0.17 0.02	0.20 0.05	0.20 0.06	0.34 0.06	0.08 0.00
NSFE	1.27 0.45	3.25 2.70		4.29 3.09		3.01 2.03	11.4 8.92	1.34 1.06		0.25 0.04	0.47 0.00	0.40 0.14	0.21 0.08
CMOA		2.65 2.13		4.83 3.46			10.47 9.00	1.14 0.95					
CMOI	0.24 0.10	2.84 1.81	0.43 0.14	4.63 3.35	0.54 0.26	3.04 2.76	12.66 10.86	2.00 1.76	0.11 0.04	0.19 0.09	0.26 0.03	0.60 0.12	0.11 0.06

iations in orientation and phase from one mooring site to the next have been discarded.

As was to be expected, the tide is dominated by the  $M_2$  component, whose ellipses, calculated from measurements taken both along the survey line as well as away from it, are shown in Fig. A1. The coherency of the dominant tidal constituent ( $M_2$ ; Fig. A1) in the area justifies our choice of using only information along the survey line.

To model the tide at a given time and location along the path joining the moorings, we first compute the predicted current at each mooring site using Eq. (A1). Since the water depth changes dramatically along the survey line, we assume mass continuity and convert the predicted tidal velocities to transport, multiplying by the water depth at each mooring site. In this way, the tidal transport can be interpolated to the desired position along the survey line without being affected by the large changes in tidal velocity across the section. Cubic splines are used for the spatial interpolation. Finally, to obtain the tidal current one simply divides the transport by the local depth.

#### REFERENCES

- Aikman, F., III, H. W. Ou, and R. W. Houghton, 1988: Current variability across the New England continental shelfbreak and slope. *Contin. Shelf Res.*, **8**, 625–651.
- Barth, J. A., D. Bogucki, S. D. Pierce, and P. M. Kosro, 1998: Secondary circulation associated with a shelfbreak front. *Geophys. Res. Lett.*, **25**, 2761–2764.
- Beardsley, R. C., and C. N. Flagg, 1976: The water structure, mean currents, and shelf-water/slopewater front on the New England continental shelf. *Mem. Soc. Roy. Sci. Liege*, **6**, 209–225.
- , D. C. Chapman, K. H. Brink, S. R. Ramp, and R. Schlitz, 1985: The Nantucket Shoals Flux Experiment (NSFE79). Part I: A basic description of the current and temperature variability. *J. Phys. Oceanogr.*, **15**, 713–748.
- Burrage, D. M., and R. W. Garvine, 1987: Supertidal frequency internal waves on the continental shelf south of New England. *J. Phys. Oceanogr.*, **17**, 808–819.
- Chapman, D. C., and R. C. Beardsley, 1989: On the origin of shelf water in the Middle Atlantic Bight. *J. Phys. Oceanogr.*, **19**, 384–391.
- , and S. J. Lentz, 1994: Trapping of a coastal density front by the bottom boundary layer. *J. Phys. Oceanogr.*, **24**, 1464–1479.
- Flagg, C. N., and B. C. Beardsley, 1978: On the stability of the shelf water/slope-water front south of New England. *J. Geophys. Res.*, **83**, 4623–4631.
- Foreman, M. G. G., 1978: Manual for tidal currents analysis and prediction (revised 1996). Pacific Marine Science Rep. 78-6, Institute of Ocean Sciences, Patricia Bay, Sidney, B.C., Canada, 57 pp.
- Galbraith, N., A. Phredemann, S. Lentz, S. Anderson, M. Baumgartner, and J. Edson, 1999: Coastal Mixing and Optics Experiment moored array data report. Woods Hole Oceanographic Institution Rep. WHOI-99-15, 156 pp.
- Garrett, C., 1972: Tidal resonance in the Bay of Fundy and Gulf of Maine. *Nature*, **238**, 441–443.
- Garvine, R. W., K.-C. Wong, G. G. Gawarkiewicz, R. K. McCarthy, R. W. Houghton, and F. Aikman III, 1988: The morphology of shelfbreak eddies. *J. Geophys. Res.*, **93**, 15 593–15 607.
- Gawarkiewicz, G., 1991: Linear stability models of shelfbreak fronts. *J. Phys. Oceanogr.*, **21**, 471–488.
- , and D. C. Chapman, 1992: The role of stratification in the formation and maintenance of shelf-break fronts. *J. Phys. Oceanogr.*, **22**, 753–772.
- , T. G. Ferdelman, T. M. Church, and G. W. Luther III, 1996: Shelfbreak frontal structure on the continental shelf north of Cape Hatteras. *Contin. Shelf Res.*, **16**, 1751–1773.
- , F. Bahr, R. C. Beardsley, and K. H. Brink, 2001: Interaction of a slope eddy with the shelfbreak front in the Middle Atlantic Bight. *J. Phys. Oceanogr.*, in press.
- Gill, A. E., 1982: *Atmosphere–Ocean Dynamics*. Academic Press, 662 pp.
- Halkin, D., and T. Rossby, 1985: The structure and transport of the Gulf Stream at 73°W. *J. Phys. Oceanogr.*, **15**, 1439–1452.
- Halliwell, G. R., and C. N. K. Mooers, 1979: The space–time structure and variability of the shelf water–slope water and Gulf Stream surface temperature fronts and associated warm-core eddies. *J. Geophys. Res.*, **84**, 7707–7725.
- Houghton, R. W., 1997: Lagrangian flow at the foot of a shelfbreak front using a dye tracer injected into the bottom boundary layer. *Geophys. Res. Lett.*, **24**, 2035–2038.
- , and M. Visbeck, 1998: Upwelling and convergence in the Middle Atlantic Bight shelf break front. *Geophys. Res. Lett.*, **25**, 2765–2768.
- , D. B. Olson, and P. J. Celone, 1986: Observation of an anticyclonic eddy near the continental shelfbreak south of New England. *J. Phys. Oceanogr.*, **16**, 60–71.
- , F. Aikman III, and H. W. Ou, 1988: Shelf–slope frontal structure and cross-shelf exchange at the New England shelfbreak. *Contin. Shelf Res.*, **8**, 687–710.
- Joyce, T. M., J. K. B. Bishop, and O. B. Brown, 1992: Observations of offshore shelf water transport induced by a warm-core ring. *Deep-Sea Res.*, **39A** (Suppl. 1), S97–S113.
- Linder, C. A., and G. Gawarkiewicz, 1998: A climatology of the shelfbreak front in the Middle Atlantic Bight. *J. Geophys. Res.*, **103**, 18 405–18 423.
- Loder, J. W., B. Petrie, and G. Gawarkiewicz, 1998: The coastal ocean off northeastern North America. A large-scale view. *The Sea*, A. R. Robinson and K. H. Brink, Eds., 105–133 pp.
- Lozier, S., and G. Gawarkiewicz, 2001: Cross-frontal exchange in the Mid-Atlantic Bight as evidenced by surface drifters. *J. Phys. Oceanogr.*, **31**, 2498–2551.
- , M. S. C. Reed, and G. Gawarkiewicz, 2001: Instability of a shelfbreak front. *J. Phys. Oceanogr.*, submitted.
- Moody, J. A., and Coauthors, 1984: Atlas of tidal elevation and current observations on the northeast American continental shelf and slope. *U. S. Geological Survey Bulletin*, No. 1611, 122 pp.
- Petrie, B., and K. Drinkwater, 1993: Temperature and salinity variability on the Scotian Shelf and in the Gulf of Maine 1945–1990. *J. Geophys. Res.*, **98**, 20 079–20 089.
- Pickart, R. S., 2000: Bottom boundary layer structure and detachment in the shelfbreak jet of the Middle Atlantic Bight. *J. Phys. Oceanogr.*, **30**, 2668–2686.
- , T. K. Mckee, D. J. Torres, and S. A. Harrington, 1999a: Mean structure and interannual variability of the slopewater system south of Newfoundland. *J. Phys. Oceanogr.*, **29**, 2541–2558.
- , D. J. Torres, T. K. Mckee, M. J. Caruso, and J. E. Przystup, 1999b: Diagnosing a meander of the shelfbreak current in the Middle Atlantic Bight. *J. Geophys. Res.*, **104**, 3121–3132.
- Pollard, R. T., and L. A. Regier, 1992: Vorticity and vertical circulation at an ocean front. *J. Phys. Oceanogr.*, **22**, 609–625.
- Ramp, S. R., R. C. Beardsley, and R. Legeckis, 1983: An observation of frontal wave development on a shelf-slope/warm core ring front near the shelf break south of New England. *J. Phys. Oceanogr.*, **13**, 907–912.
- Twicheil, D. C., C. E. McClennen, and B. Butman, 1981: Morphology and processes associated with the accumulation of the fine-grained sediment deposit on the southern New England shelf. *J. Sediment. Petrol.*, **51**, 269–280.